Temporal Dynamics of Groundwater Flow Direction in a Glaciated, Headwater Catchment

Joshua Robert Benton

Thesis submitted to the faculty of the Virginia Polytechnic Institute and State University in partial fulfillment of the requirements for the degree of

Master of Science

In

Geosciences

Madeline E. Schreiber, Chair

Kevin J. McGuire

Scott W. Bailey

Ryan M. Pollyea

May 12, 2020

Blacksburg, VA

Keywords: solum, c horizon, soils, critical zone, watershed, hydraulic gradients, glacial till, spodosol

Temporal Dynamics of Groundwater Flow Direction in a Glaciated, Headwater Catchment

Joshua Robert Benton

ABSTRACT

Shallow groundwater flow in the critical zone of steep headwater mountain catchments is often assumed to mimic surface topography. However, groundwater flow is influenced by other variables, such as the elevation of the water table and subsurface hydraulic conductivity, which can result in temporal variations in both magnitude and direction of flow. In this study, I investigated the temporal variability of groundwater flow in the soil zone (solum) within the critical zone of a headwater catchment at the Hubbard Brook Experimental Forest in North Woodstock, NH. Groundwater levels were continuously monitored throughout several seasons (March 2019 to Jan 2020) in a network of wells comprising three hillslope transects within the upper hillslopes of the catchment. Five clusters of three wells per cluster were screened from 0.18 – 1.1 m depth at the base of the solum. Water levels were also monitored in five deeper wells, screened from 2.4 - 6.9 m depth within glacial sediments of the C horizon. I conducted 47 slug tests across the well network to determine hydraulic properties of the aquifer materials surrounding each well. In addition, our team conducted a large-scale auger investigation mapping soil horizon depths and thicknesses.

Results show that the magnitude of hydraulic gradients and subsurface hydrologic fluxes varied at each site with respect to changing water-table elevation, having a maximum range of 0.12 m/m and 9.19 x 10^{-6} m/s, respectively. The direction of groundwater flow had an arithmetic mean deviating from surface topography by 2-10 degrees, and a total range that deviated from surface topography by as much as 51 degrees. During lower water table regimes, groundwater flow direction deviated from the ground surface, but under higher water table regimes, in response to recharge events, flow direction mimicked surface topography. Within most of the well clusters, there is an observable connection between the slope direction of the top of the C horizon and the direction of groundwater flow during lower water table regimes. Slug test results show the interquartile range of saturated hydraulic conductivity (K_{sat}) within the C horizon

(1.5×10^{-7} to 9.8×10^{-7} m/s) is two orders of magnitude lower than the interquartile range of K_{sat} values within the solum (2.9×10^{-5} to 5.2×10^{-5} m/s). Thus, the C horizon is on average a confining unit relative to the solum that may constrict groundwater flow below the solum. Additionally, results from the larger scale auger investigation suggest that deviations in subsurface topography of the C horizon may be generalizable at the larger hillslope scale. Overall, these results indicate that 1) shallow groundwater flow direction and magnitude within this headwater catchment are dynamic and can deviate from surface topography, and 2) the subsurface topography of the C horizon can influence groundwater flow direction. These results imply that temporal dynamics of groundwater flow direction and magnitude should be considered when characterizing subsurface flow in critical zone studies. Additionally, knowledge of subsurface topography of confining units may provide constraints on the temporal variability of groundwater flow direction.

Temporal Dynamics of Groundwater Flow Direction in a Glaciated, Headwater Catchment

Joshua Robert Benton

GENERAL AUDIENCE ABSTRACT

Streams that originate at higher elevations (defined as headwater streams) are important drinking water sources and deliver water and nutrients to maintain freshwater ecosystems. Groundwater is a major source of water to these streams, but little is known about how groundwater flows in these areas. Scientists delineate watersheds (areas of land that drain water to the same point) using surface topography. This approach works well for surface water, but not as well for groundwater, as groundwater may not flow in the same direction as surface water. Thus, assuming that the ground-watershed is the same as the surface watershed can lead to errors in hydrologic studies.

To obtain more accurate information about groundwater flow in headwater areas, I continuously measured groundwater levels in forest soils at the Hubbard Brook Experimental Forest in North Woodstock, NH. My main objective was to determine if there is variability in the direction and amount of groundwater flow. I also measured the characteristics of the soils to identify the thicknesses of soil units and the permeability of those units. I used these data to evaluate the relationship between groundwater flow direction, surface topography, and the permeability of soil units.

Overall, I found that groundwater flow direction can differ significantly from surface topography, and groundwater flow direction was influenced by the groundwater levels. When groundwater levels were high (closer to the land surface), groundwater flow was generally in the same direction as surface topography. However, when groundwater levels were lower, flow direction typically followed the slope of the lowest permeability soil unit. These results suggest that scientists should not assume that groundwater flow follows the land surface topography and should directly measure groundwater levels to determine flow direction. In addition, results from this study show that characterizing soil permeability can help scientists make more accurate measurements of groundwater flow.

Dedication

This thesis is dedicated to the memory of my late father, Wendell Lee Benton, who lived every moment to the fullest and found joy in whatever he did.

Acknowledgements

First and foremost, I would like to thank my advisor and committee chair, Madeline Schreiber, who took me on as a student and provided me with the opportunity to contribute to this project. Maddy's excellent mentorship, hard work, constant feedback, and patience have been invaluable to me throughout this process and I am grateful for having this opportunity to learn from her and collaborate with her.

I would like to express my appreciation to my committee members, Kevin McGuire, Scott Bailey, and Ryan Pollyea, for spending hours with me in the field, classroom, and office providing feedback, bouncing ideas, and bestowing knowledge that has been instrumental to this project.

Thanks to the entire Hubbard Brook team including a consortium of faculty, graduate students, and undergraduate students who have contributed and played a major role in making this project possible. This includes Brian Strahm, Don Ross, Amanda Pennino, Jennifer Bower, Stephanie Duston, Nathanial Rasnake, Delaney Peterson, Michaela Kuhn, Kinsey Ashe, and JP Gannon. I cannot thank this group enough for all their hard work and contributions.

Thanks to my mother and father, Jane Anderson and Wendell Benton, for supporting me in my pursuits of higher education, and for teaching me the importance of hard work while also teaching me the value of slowing down to stop and enjoy life.

I would like to thank my wife, Kristi Wright, for her constant support, patience, and understanding while I had to spend many days away from home while pursuing both graduate and undergraduate studies. Thank you for always being there for me during both the good times and the challenging times.

Thanks to my mentors and friends, Daniel Doctor and Callan Bentley, who were instrumental in preparing me for graduate school. I would also like to thank my Blacksburg family, Wil Orndorff, and Zenah Orndorff, for their support and friendship throughout my graduate studies.

This project was supported by the National Science Foundation (Grant #1643327), and the Department of Geosciences at Virginia Tech.

Table of Contents

1.0 Introduction

Headwater streams play a critical role in nutrient cycling and maintaining biodiversity in freshwater ecosystems (Clarke, 2008). In addition, headwater streams are important water supplies; over a third of the U.S. population relies on the low-order streams in headwater catchments for drinking water (Alexander et al., 2018; Sills et al., 2018). Furthermore, headwater drainage networks comprise more than 50% of the total stream length within the contiguous U.S. (Datry et al., 2014; Jensen et al., 2019, Nadeau and Rains, 2007) and influence downstream surface water quality (Alexander et al., 2007), highlighting the importance of headwater systems in water resource management (Lowe and Likens, 2005; Wohl, 2017).

A growing body of literature emphasizes that groundwater is a major component in a multitude of hydrologic processes in headwater catchments. Groundwater is a dominant source of water for many streams, particularly in humid regions (Winter et al., 1999). Groundwater contributes to streamflow via base-flow, which allows for sustained flow during dry periods, and storm flow, which contributes to increases in stream discharge in response to recharge events (Winter et al., 1999). As a result, many of the chemical and physical characteristics of headwater streams are intrinsically connected to their surrounding catchment by the groundwater flow paths that deliver water and solutes from the hillslopes to the stream network. For example, Zimmer et al. (2013) demonstrated that the spatial and temporal variability of chemistry within a headwater stream was connected to groundwater within the adjacent hillslopes. During periods of high flow, stream chemistry reflected the chemical variability of shallow groundwater, while during low flow, it was controlled by inputs from groundwater seeps that increased both the pH and concentrations of base cations (Zimmer et al, 2013).

Groundwater also plays an important role in controlling runoff generation (Haught and Tromp-van Meerveld, 2011; Penna et al., 2015), determining the timing and degree of connectivity between hillslopes and streams (Detty and McGuire 2010b), and influencing pedogenic processes within catchment soils (Bailey et al. 2019). All these processes are influenced by variability in groundwater flow paths, highlighting the need for characterizing these flow paths for predicting the physical and chemical response of headwater streams to both land disturbances and changes in climate inputs within catchment boundaries.

1.1 Groundwater basins

Headwater catchments are typically delineated using land surface topographic contours (Gillin et al., 2015; Young et al., 2019; Voeckler et al., 2014). This method of catchment delineation has underpinned small catchment studies for decades, including those utilizing mass balance to determine solute and hydrologic fluxes through gauged catchments (Bormann and Likens, 1967; Bailey et al., 2003). The topographically based method of catchment delineation assumes that subsurface (groundwater) drainage follows surface topography. However, this assumption can lead to significant error when estimating the contributing area to a stream if groundwater flow paths deviate from the land surface, implying that groundwater basin divides do not correspond to land surface divides (Hinton and Schiff, 1993).

Groundwater basins, the portion of the saturated subsurface contributing drainage to a receiving body of water, are delineated by water-table contours (Panno and Luman, 2018, Hinton and Schiff, 1993, Dunlap and Spinazola, 1984). As a result, groundwater basin delineation relies on physical measurements of the depth to the water table using piezometers or wells and an interpolation method such as kriging to estimate water table elevation in regions without physical measurements (Dunlap and Spinazola, 1984). The accuracy of interpolated water-table elevation values is determined by the spatial distribution of points of known values (Nikroo, 2009) that are limited to locations of wells, piezometers, and surface expressions of the water table such as seeps, springs, and gaining streams. As a result of the limited number of observations, groundwater basins are often difficult and expensive to characterize.

Over the past decade, due to an increase in the affordability and diversity of water level data loggers, high-frequency measurements of groundwater levels in headwater catchments have increased (see examples in Detty and McGuire, 2010a; Tromp-van Meerveld et al. 2015), shedding new light on previously unknown spatiotemporal dynamics of saturated groundwater flow within headwater catchments. Collection of high-frequency observational data can improve the predication capabilities of hydrologic models (Kirchner, 2005), especially during non-stationary times (Burt and McDonnell, 2015).

1.2 Groundwater flow in headwater catchments

Groundwater flow within headwater catchments is composed of both storm flow (throughflow) and deeper groundwater flow (Carroll et al., 2019) where throughflow is often conceptualized as saturation separated from the deeper groundwater components contributing to streamflow (Robinson and Ward, 2017). Throughflow has short residence times (hours to days) whereas deeper groundwater flow can have longer residence times (months to years). Throughflow can be a dominant source of runoff generation during storm events comprising a large volume of streamflow (Weiler et al. 2005); however, the relative contribution of throughflow to streamflow varies depending upon a multitude of factors including antecedent soil moisture conditions, characteristics of soil and underlying geologic materials, and morphology of the basin (Chifflard et al., 2019).

The generation of throughflow has been proposed to occur as a result of two mechanisms: 1) perched saturation (Carroll, 2019, Heller and Kleber, 2016) developing on top of low permeability subsurface layers, or 2) deeper water tables rising into shallow, higher permeability soils (transmissivity feedback) (Hjerdt, 2002). Perched saturation develops at abrupt changes in permeability at the soil-to-bedrock interface or above low permeability soil units. Transmissivity feedback in soils occurs as the result of an observed exponential decrease in hydraulic conductivity with increasing depth (Rinderer and Seibert, 2012) producing an exponential increase in transmissivity and groundwater discharge as water table elevations rise towards the land surface. Both mechanisms result in a lateral flux of groundwater traveling downslope in response to storm events. Once generated, throughflow can have a wide range of downslope travel distances (Klaus and Jackson, 2018) before infiltrating into the underlying impending layer. Therefore, throughflow generated within upper hillslopes of headwater catchments can have a wide range of connectivity to downslope riparian zones contributing groundwater to streams. While the behavior of throughflow on trenched hillslopes has been studied in previous work (Tromp-van Meerveld and McDonnell, 2006, Uchida et al., 2005), the dominant mechanism of throughflow development (perched versus transmissivity feedback) in upland, glaciated settings has not been well documented.

Groundwater flow direction within headwater catchments is dynamic. When Rodhe and Seibert (2010) investigated the dynamics of groundwater flow direction within soils in a till-

mantled watershed, they observed a significant amount of variability in flow direction through time; flow direction was most variable in the riparian zone and least variable on the upper hillslopes. During high water tables, the flow direction in the riparian zone was perpendicular to the direction of stream flow while under lower groundwater levels, flow direction was parallel to it. In contrast, while investigating groundwater flow direction in a headwater catchment comprising of clay rich soils directly overlying bedrock, Tromp-van Meerveld et al. (2015) observed the least amount of variability in flow direction in the riparian zones and more variability in the hillslopes adjacent to depressions within bedrock topography. Tromp-van Meerveld et al. (2015) also observed a strong, positive correlation between groundwater flow direction during lower water-table regimes and the topography of the bedrock.

In addition to bedrock topography, groundwater flow in headwater catchments may also be influenced by the topography of subsurface confining units. In a study in a till-mantled hillslope, Hutchinson and Moore (2000) found that hydraulic gradients (and inferred groundwater flow direction) in shallow soils follow the topography of the underlying lower-permeability glacial till. Other studies have shown that soil permeability can vary with depth; for example, in the till-mantled headwater catchments of the Hubbard Brook (NH) watershed, hydraulic conductivity of unconsolidated soils overlying glacial sediments has been shown to decrease with depth (Detty and McGuire, 2010a, Burns, 2012). However, to date, few studies have addressed the specific influence of soil permeability contrasts or subsurface topography of confining units on flow direction in these settings.

In this thesis, I investigate relationships between groundwater flow direction and water-table elevation, permeability contrasts within subsurface materials, and surface and subsurface topography in a glaciated headwater catchment at the Hubbard Brook (NH) watershed. I focus specifically on the influence of permeability contrasts in soils and the subsurface topography of lower permeability units on hydraulic gradients and groundwater flow direction. To do this, I use high-frequency temporal measurements (1-10 min logging interval) of water-table elevations recorded at multiple depths (both in high permeability and low permeability soil units) within three hillslope transects over a 10-month period, combined with measurements of hydraulic conductivity of the underlying soil units, and estimated elevations and thicknesses of the soil units to address the following questions:

1.) Does groundwater flow direction and magnitude vary through time and space in the soils of a headwater catchment?

2.) What are the drivers influencing the variability of groundwater flow direction?

1.3 Site description

This study was conducted in Watershed 3 (WS3), a south-facing, gauged watershed within the Hubbard Brook Experimental Forest (HBEF) in North Woodstock, NH (Figure 1) that encompasses the headwaters for Paradise Brook, a perennial first-order headwater stream (Zimmer et al., 2013). WS3 is the hydrologic reference watershed for a series of paired watershed vegetation removal experiments (Hornbeck et al. 1970) designed to study headwater streamflow response to deforestation (Likens et al. 1970). As the control, WS3 was left relatively undisturbed, has not been logged since late 1910s and has maintained an approximate steady-state biomass since the 1980s (Likens, 2013). The Hubbard Brook Valley is covered by a northern hardwood forest comprised of American Beech (*Fagus grandifolia*), sugar maple (*Acer saccharum*), and yellow birch (*Betula alleghaniensis*) dominating mid-lower elevations (500-750 MSL), and balsam fir (*Abies balsamea*), red spruce (*Picearubens*), and white birch *(Betula papyrifera* var. *cordifolia*) dominating higher elevation portions of the catchment greater than 750 MSL (Likens, 2013).

WS3 is underlain by metasedimentary sillimanite grade, pelitic schists of the upper Rangeley Formation exhibiting steeply dipping foliation that strikes dominantly NE-SW and steeply dipping fracture sets that also have a preferred NE strike orientation (Burton et al., 2000). The Rangeley Formation is overlain by glacial sediments of varied thickness deposited during Wisconsin glaciation in the late Pleistocene (Bailey et al., 2014) (Figure 1b). These glacial deposits are primarily sandy loams that are discontinuous and thinner within the upper portions of the catchment dominated by bedrock outcrops. The glacial deposits consist of both basal tills (loams) and lenses of sand, resulting in spatially heterogenous permeability architecture (Bailey et al. 2014) comprising the C horizon.

Soils within WS3 are spodosols with an average thickness of 0.5 meter (Likens, 2013). Soil development and horizonation (development of soil horizons) at HBEF has both a lateral and vertical component, leading to distinct soil units and a predictable spatial architecture of

spodic horizons across different landscape positions (Bailey et al., 2014). For example, within the upland portions of the catchment, particularly in convergent zones adjacent to bedrock outcrops, soils have a thicker E horizon relative to other horizons; further downslope, however, soils overlying glacial deposits tend to have thicker B horizons relative to other horizons. A multitude of these distinct soil morphological units defined by relative horizon thickness have been identified and mapped within WS3. Gannon et al. (2014) showed that these soil units correlate to distinct water-table regimes, such as saturation frequency and threshold response to changes in catchment storage.

The climate of WS3 is classified as humid continental with a mean annual precipitation of 140 cm evenly distributed throughout the year. Approximately one-third to one-quarter of this precipitation occurs as snowfall (Bailey et al., 2003). WS3 has a total elevation change of 205 m with an average slope of 28% (Likens, 2013).

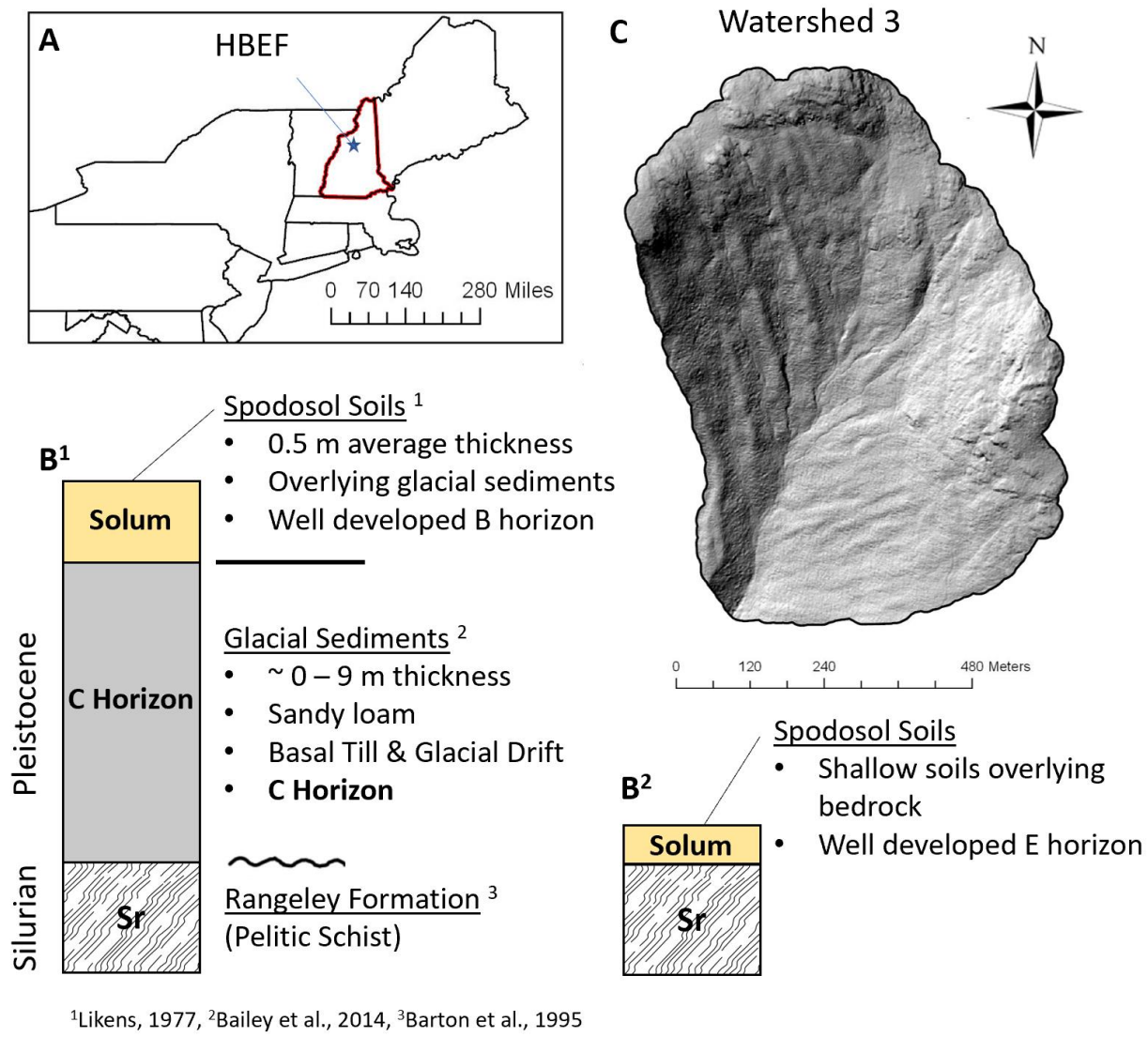

Figure 1.A: Map showing the location of the Hubbard Brook Experimental Forest and Watershed 3. Figure 1.B: Stratigraphic columns (not drawn to scale) showing the surficial deposits overlying bedrock at two example locations ($B^1$and B^2) within Watershed 3. At location B^1 ,typical of lower elevations of WS3, Pleistocene glacial sediments comprising the C horizon sit unconformably on top of the fractured, crystalline bedrock of the Rangeley Formation, and the solum is the weathered portion of the glacial sediments that has undergone significant alteration as a result of soil-forming processes. At location B^2, typical of higher elevations of WS3, shallow organic rich soils with well-developed E horizons directly overly bedrock. Figure 1.C Lidar-derived hillshade digital elevation model (DEM) of Watershed 3 highlighting the drainage network, and the variation in topography across the catchment. The east-facing slope has well defined valleys and ridges while the west-facing slope has a more planar topography.

2.0 Methods

2.1 Well network and survey

The instrumentation design for this project was in support of a larger, multidisciplinary project investigating spatial gradients in chemical weathering rates within glaciated, headwater catchments. One goal of the larger project was to estimate solute fluxes in groundwater over different hydrologic periods. To do this, the research team designed and installed a 28 groundwater well network in transects within the upper reaches of WS3 where the largest gradients in chemical weathering rates were hypothesized to be located.

This well network consists of three hillslope transects (Figure 2: Transects 42, 52, & 86) located within subcatchments of WS3. Transects 42 & 52 are at higher elevations on the east facing slope, 713 – 667 meters above mean sea level (MASL); transect 86 is on the west facing slope, at a lower elevation (604 – 618 MASL). The overall well network contains 20 shallow wells (0.18 – 1.1 m depth) screened within the solum, and 6 deep wells (2.4 – 6.9 m depth) screened within the C horizon (Figure 2). The solum encompasses all the soil horizons above the C horizon and the base of the solum is also the approximate depth of the rooting zone in WS3. Within the shallow well network, there are five well clusters of three wells per cluster (Figure 3) used for determining the magnitude and direction of the hydraulic gradient. The wells within each cluster are spaced near each other (within 8 m) to minimize the risks of measuring hydrologically disconnected water-tables within an aquifer that is highly dissected by irregularly undulating bedrock topography.

At higher elevations, shallow wells were installed within the solum (screened within the E horizon) directly overlying bedrock (Figure $1B^2$), and at lower elevations shallow wells were installed within the solum (screened within the B horizon) directly overlying C horizon (Figure $1B^1$). In addition to the transect wells, other shallow wells were also installed within the B horizon overlying glacial sediments in other areas of WS3 (Figure 2). An example cross-section of a well transect illustrates the transition from the upslope bedrock dominated portions of WS3 to the downslope thickening wedge of glacial sediments comprising the C horizon (Figure 4).

The well network was surveyed with a Leica © Total Station theodolite at 1 mm ± 1 ppm measurement accuracy. The properties of each well cluster are summarized in Table 1, and the properties of each individual well are summarized within Table 2.

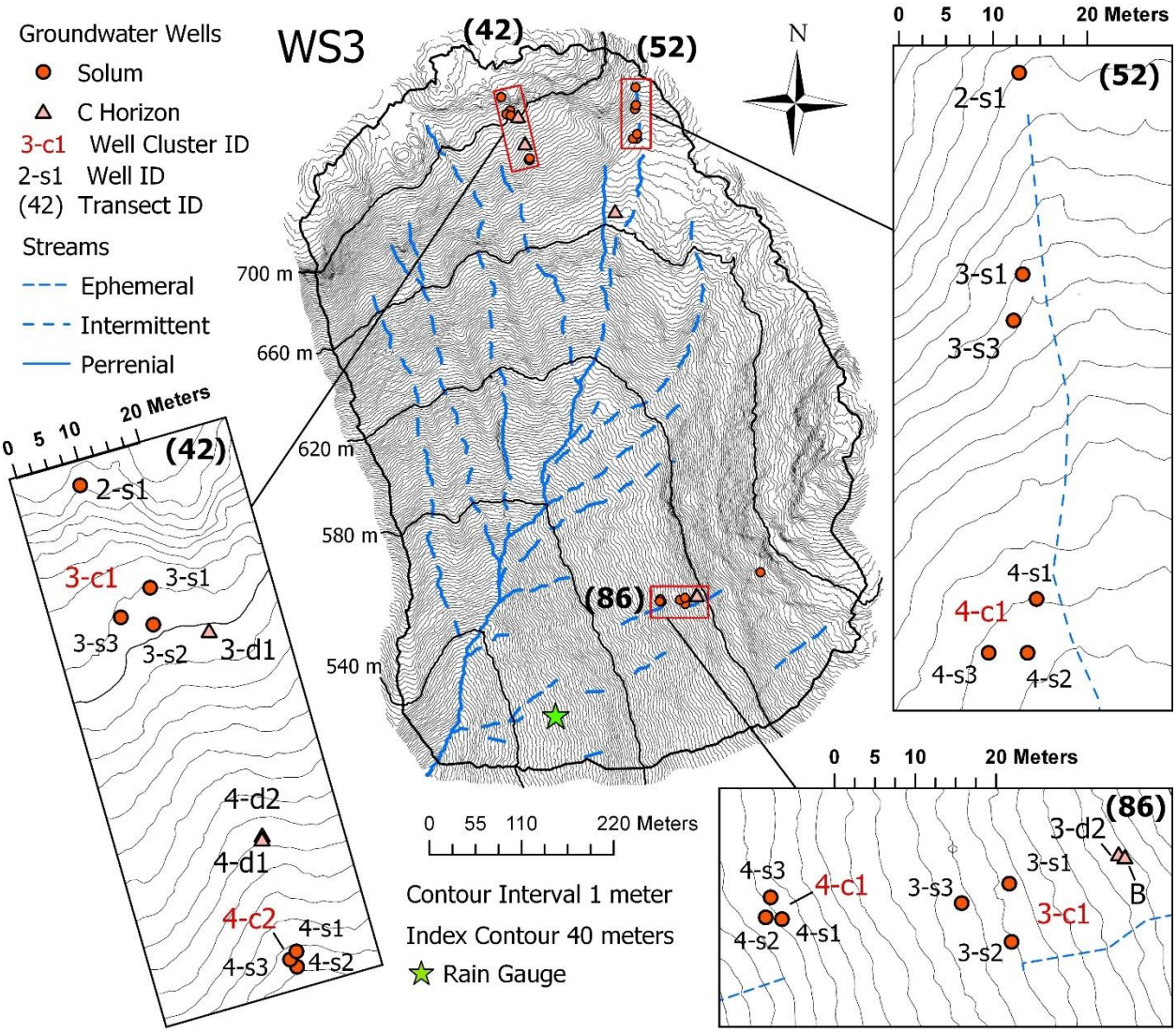

Figure 2: A topographic map of WS3 with the locations of each well transect (42,53, & 86) where groundwater wells are symbolized by the stratum in which the screened interval is installed in. The wells are separted by shallow wells installed within the solum (red circles), and deeper wells installed within the C horizon (orange triangles). The location of the barometric logger is at the top of a deep well at (86)-B, and the location of the rain gauge is indicated by a green star. The surface drainange network is represented by solid blue lines (perennial streams) and dashed blue lines (intermittent & ephemeral streams).

Figure 3: A cluster of shallow groundwater wells, (86)-4-c1, installed within the solum used for flow direction and hydraulic gradient calculations.

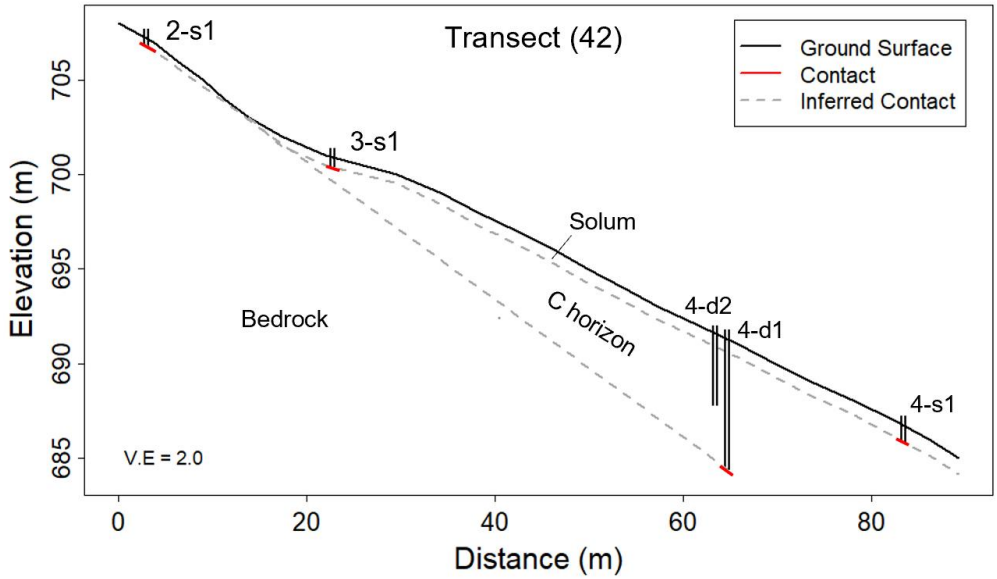

Figure 4: A cross-section of Transect (42) with the locations and depths of select wells, and contacts between bedrock, C horizon, and the solum. Well 2-s1 is installed within the solum directly overlying bedrock.

Table 1: A table describing the properties of five triangles formed at the ground surface by each cluster of wells. This includes geometric properties of each triangle (perimeter and area), the maximum change in elevation over horizontal distance (slope), and the maximum slope direction relative to North (aspect). Additionally, the average depth of the base of each well (relative to ground surface) within a given cluster is included.

Well Cluster ID	Perimeter (m)	Area (m^2)	Slope (m/m)	Azimuth (degrees)	Mean Well Depth (m)
(42)-3-c1	15.51	11.49	0.12	139	0.67
(42)-4-c1	11.39	5.06	0.27	161	0.89
(52)-4-c1	13.39	6.97	0.16	133	0.61
(86)-3-c1	20.98	20.64	0.25	246	0.67
(86)-4-c1	7.84	2.77	0.23	242	0.74

2.2 Well construction, installation & development

The shallow wells were constructed using 2-inch diameter solid PVC attached to 2-inch diameter PVC screen (0.010 slot size). The screened interval was 30.48 cm for wells in the B horizon, and 15.24 cm for wells in the E horizon. Solum wells were installed using a 3-inch diameter bucket auger. Once the well was seated in place within the borehole, the annular space was backfilled with the filter pack (sand) to approximately 2.5 cm above the top of screened interval (Figure 5). A combination of locally derived sand and industrially sourced silica sand was used for the filter pack. The type of filter pack sand was kept consistent between wells within a given cluster. The locally sourced sand was obtained from quarries in glaciofluvial deposits; the material was sieved to exclude grain size diameters smaller than 0.5 mm (U.S. Standard Sieve #35) and coarser than 2 mm (U.S. Standard Sieve #35). Above the filter pack, the annular space was backfilled with the native soil removed during the borehole excavation. A plastic flange was tightly wrapped around each well and placed at the top of the soil backfill to mitigate surface infiltration and preferential flow around the well.

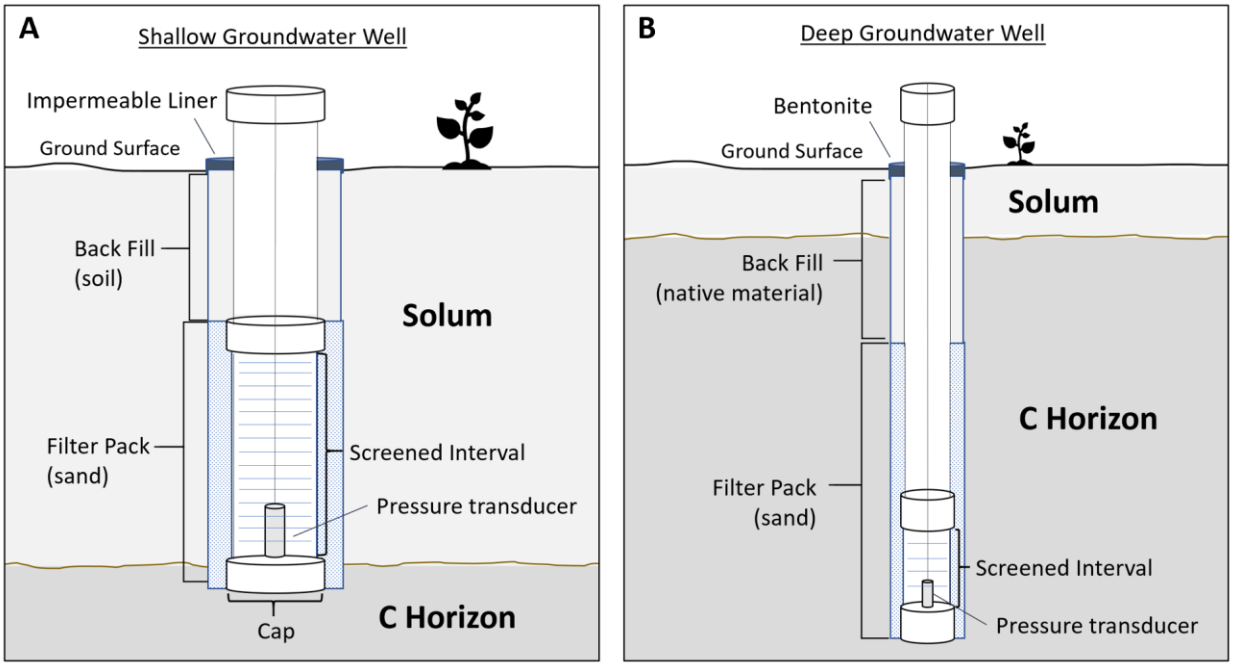

Figure 5A: A schematic cross section of a shallow well screened within the solum directly above the interface between the solum and the C horizon. Figure 5B: A schematic cross section showing an example of a deep well installed within the middle portion of the C horizon. Note: Figures are representative of multiple wells and are not drawn to scale.

The deep wells screened within the C Horizon were installed using a track-mounted drill rig using hollow-stem augers. Wells were constructed with 2" PVC and screen (0.010 slot size); the annular space surrounding the well screen was filled with #1 silica sand to approximately 0.2 – 0.5 meters above the top of the screened interval, and 00 sand to approximately 1 meter above the top of the screened interval. Above this, native material was backfilled above the sand, and bentonite was added to 1-2 ft below surface. Details of deep wells are presented in Table 2.

All wells were developed using surging and pumping methods after installation. If the well was dry after installation, water was poured into the well and then pumped back out multiple times until the water appeared clear.

2.3 Installation of water level loggers

Pressure transducers (HOBO © Onset U20 & U20L data loggers) were installed within each well to measure water levels at 1-10-minute logging intervals. The pressure transducers were suspended immediately above the base of the well (Figure 4) by a 20-pound test monofilament line attached to the vented cap of the well. To measure barometric pressure in the

watershed, we installed an additional transducer within the PVC casing of one of the deeper wells. Raw pressure data obtained from the transducers were converted to water level by compensating for barometric pressure and reference water level measurements using Onset® HOBOware® graphing and analysis software.

Manual measurements of the water-table within each well were also collected throughout the study period using a Solinst ® water level meter (1/1000 ft ± .01 ft measurement accuracy) prior to installation of the loggers, before the removal of loggers for data retrieval, and during aquifer tests.

2.4 Measurement of hydraulic conductivity

The saturated hydraulic conductivity of the aquifer material surrounding each well was estimated using the Hvorslev method of analyzing rising head slug test data (Hvorslev, 1957). The majority of slug tests were conducted May, 2019 when water-tables were relatively high across the well network. A total of 47 slug tests were conducted across the entire well network, with at least two slug tests conducted for each shallow well.

For each slug test, a rapid displacement of the water-table was initiated by pumping water out of the well; the recovery of the water-table was recorded at one-second logging intervals until the water-table re-equilibrated to background conditions. Relative head values for each slug test were plotted on a semi-log scale (Figure S1), and an ordinary least squares regression was applied to the log-transformed data in order to determine the basic time lag (t_{37}). The basic time lag (t_{37}), length of the well screen (L), radius of well casing (r_c), and the radius of the well including the filter pack (r_w) were input into equation 1 for determining saturated hydraulic conductivity (K_{sat}). Equation 1 is the general solution for K_{sat} assuming the length of the well screen (L) is greater than eight times the radius of the well including the filter pack (r_w) (Hvorslev, 1957).

$$K_{sat} = \frac{{r_c}^2 \cdot \ln\left(\frac{L}{r_w}\right)}{2 \cdot L \cdot t_{37}} \; ; \; \frac{L}{r_w} > 8 \qquad \textbf{(1)}$$

Table 2: Table showing the length of the screened interval (screen length), depth to the base of the screened interval (screen depth), screened horizon, and the soil horizon or interface that the base of the well is seated upon.

Well ID	Screen Length (m)	Screen Depth (m)	Screened Horizon	Base of Well
(42)-2-s1	0.15	0.33	E	Bedrock
(42)-3-s1	0.30	0.46	BC	B/C Interface
(42)-3-s2	0.30	1.05	BC	B/C Interface
(42)-3-s3	0.30	0.53	BC	B/C Interface
(42)-3-d1	0.31	2.67	C	C Horizon
(42)-4-s1	0.30	0.84	BC	B/C Interface
(42)-4-s2	0.30	0.88	BC	B/C Interface
(42)-4-s3	0.30	0.91	BC	B/C Interface
(42)-4-d1	0.61	6.86	Bedrock surface	Bedrock
(42)-4-d2	0.61	3.71	C	C Horizon
(52)-2-s1	0.15	0.37	E	Bedrock
(52)-3-s1	0.30	0.56	Bhs	Bhs Horizon
(52)-3-s2	0.30	0.60	Bhs	Bhs Horizon
(52)-3-s3	0.30	0.51	Bhs	Bhs Horizon
(52)-4-s1	0.30	0.46	BC	B/C Interface
(52)-4-s2	0.30	0.63	BC	B/C Interface
(52)-4-s3	0.30	0.79	BC	B/C Interface
(52)-4-d2	0.61	3.05	Bedrock surface	Bedrock
(86)-3-s1	0.30	0.77	Bhs/C	B/C Interface
(86)-3-s2	0.30	0.57	Bhs/C	B/C Interface
(86)-3-s3	0.30	0.74	Bhs/C	B/C Interface
(86)-3-d2	0.61	3.05	Bedrock surface	Bedrock
(86)-4-s1	0.30	0.97	BC	B/C Interface
(86)-4-s2	0.30	0.70	BC	B/C Interface
(86)-4-s3	0.30	0.69	BC	B/C Interface

2.5 Calculation of gradients

Hydraulic Gradients

Hydraulic gradients were calculated in R statistical software package (Figure S1) using time series of water level elevation combined with the horizontal coordinates of each well, assuming

there is a linear change in head between each well. The hydraulic head (h) within three wells is expressed as three points on a plane, and a system of linear equations:

$$h_1 = a + x_1 b + y_1 c$$
$$h_2 = a + x_2 b + y_2 c$$
$$h_3 = a + x_3 b + y_3 c$$

x = longitudinal coordinate
y = latitudinal coordinate
h = elevation of water table **(2)**

This system of linear equations can be expressed in matrix form with the coefficient matrix (**A**), variable matrix (**B**), and the constant matrix (**C**).

A **B** **C**

$$\begin{bmatrix} 1 & x_1 & y_1 \\ 1 & x_2 & y_2 \\ 1 & x_3 & y_3 \end{bmatrix} \begin{bmatrix} a \\ b \\ c \end{bmatrix} = \begin{bmatrix} h_1 \\ h_2 \\ h_3 \end{bmatrix} \qquad b = \frac{\partial h}{\partial x}\ ,\ c = \frac{\partial h}{\partial y} \qquad \textbf{(3)}$$

$$\mathbf{B = A^{-1}C}$$

The unique solution to the system of linear equations, column vector **B**, is determined by multiplying the inverse of the coefficient matrix ($\mathbf{A^{-1}}$) by the column vector **C**. This yields the hydraulic gradient in the x-direction ($\frac{\partial h}{\partial x}$), and the hydraulic gradient in the y-direction ($\frac{\partial h}{\partial y}$). The magnitude of flow ($\frac{dh}{dl}$) is then determined with Pythagorean's theorem and the direction of maximum hydraulic gradient (θ) is determined by the inverse tangent function:

$$\frac{dh}{dl} = \sqrt{b^2 + c^2}, \quad \theta = \tan^{-1}\left(\frac{b}{c}\right) \qquad \textbf{(4)}$$

In accordance with Darcy's Law, I assumed that groundwater flows from high potential to low potential in the direction of the negative maximum hydraulic gradient (θ). Flow direction calculations are made at every time step in which water levels above a minimum threshold were detected within each of the three wells. After experimenting with a range of values, a threshold of 5 cm was determined to be optimal for this study. This threshold is within the operating range of the logger and above the possible ponding depth at the base of well.

Gradients of land surface and top of the C horizon:

Both the maximum horizontal gradient and slope direction (direction of maximum horizontal gradient) were determined at each well cluster for the land surface and the top of the C horizon. The C horizon was identified by Munsell color and textural characteristics consistent with methods used in previous work at Hubbard Brook (Bailey et al. 2014). The depth to the top of the C horizon was measured within each borehole excavated for well installation. The maximum gradients of the land surface and the top of the C horizon were calculated by replacing water table elevation (h) in equation 3 with the elevation of the land surface and the elevation of the top of the C horizon measured at each well location.

To identify the presence and thicknesses of soil horizons in each subcatchment, an auger investigation was conducted during the summer of 2019. Data from the survey were used for determining the gradient and slope direction of the top of the C horizon compared to the land surface across each subcatchment. The auger investigation was conducted along multiple, equally spaced transects creating a grid with a 10-meter spatial resolution. Each auger investigation went to depth of refusal, and the depths of soil horizon transitions were measured including the depth to the top of the C horizon (if the C horizon was present). The GPS locations of transect endpoints were determined using a Trimble Geoexplorer XT GPS unit with an external hurricane antenna; the GPS locations of each auger point were extrapolated from endpoint measurements. Auger locations where the C horizon was not observed were filtered (removed) from the dataset leaving a total of 30 measurements in transect 52, 37 measurements in transect 42, and 15 measurements in transect 86 used for gradient calculations of the C horizon. Within ArcGIS, a series of three-point clusters of comparable size and geometry to the well clusters were visually identified, and the maximum slope directions of the ground surface and the top of the C horizon were calculated (equation 3) for each cluster.

2.6 Calculation of hydrologic fluxes:

Hydrologic fluxes through the solum were estimated using Darcy's Law (equation 5; Darcy, 1856) for saturated water flow through a porous medium at each of the well clusters installed at the base of the solum.

$$Darcy\ flux\ (q) = -K_{sat} \cdot \frac{dh}{dl} \quad \textbf{(5)}$$

The hydrologic flux (Darcy Flux; units of L/T) is calculated by multiplying the arithmetic mean of the saturated hydraulic conductivity (L/T) determined from slug test analysis by the hydraulic gradient (L/L) (Equation 4) at 10-minute time intervals.

3.0 Results

3.1 Water table characteristics and response to recharge events

Throughout the study period (Mar. 2019 – Jan. 2020), water tables were transient within the shallow wells, rising in and out of the solum, and permanent within the deeper wells, fluctuating seasonally or on an event basis yet never dropping below the screened interval (Figure 6E). Near the ridges of the watershed, where bedrock crops out close to the surface and the solum is thin, water tables were episodic, only rising into the solum in response to rain or snow melt events (Figure 6A). Within thicker soils overlying the C horizon, water tables remained in the solum seasonally, dropping below the base of the solum in mid-summer (June-July) before rising back into the solum during the fall (Figure 6B-D). The highest water tables occurred during the spring snow melt season (March – April) that was followed by an overall recession period persisting into the early summer (June-July; Figure 6).

The timing of the water table response to precipitation events across the well network varied depending upon transect, hillslope position, and soil horizon. For example, water tables within the solum in Transects 42 and 86 (see Figure 2) exhibited longer time-lags in peak water table between different hillslope positions, while water tables within the solum in Transect 52 occurred approximately at the same time regardless of hillslope position (Figure 7).

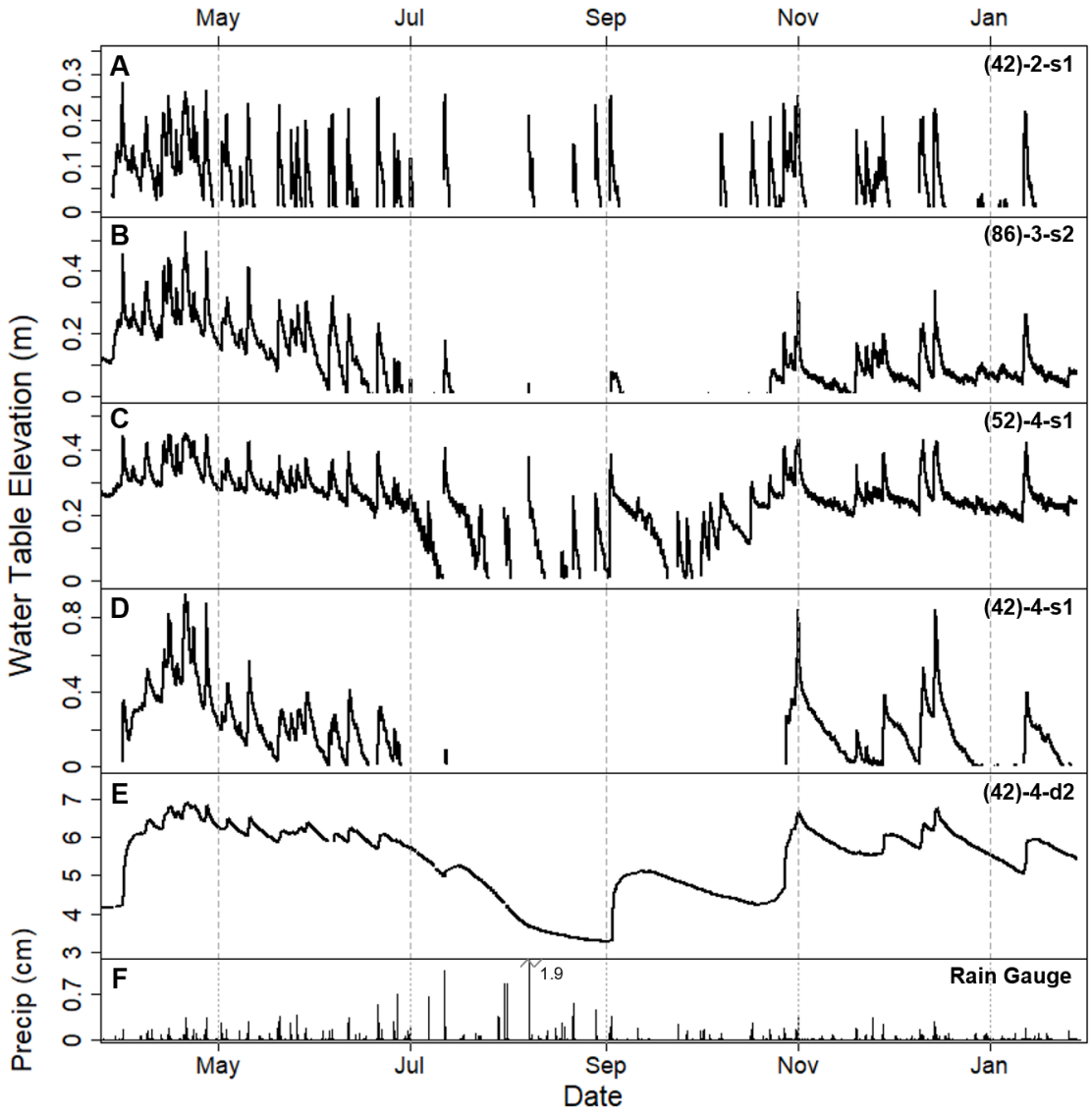

Figure 6: A time series (March 2019-Jan 2020) showing water table elevation relative to the base of the solum (Panels A-D) for three shallow wells, water table elevation relative to the base of the C horizon for a deep well (Panel E), and precipitation (Panel F). The gaps in data within the shallow wells (Panels A-D) imply that the water table is below the base of the solum ($y < 0$). Well # (42)-2-s1 is installed within shallow soil directly overlying bedrock while wells (86)-3-s2, (52)-4-s1, and (42)-4-s1 are installed within soils overlying C horizon. Well # (42)-4-d2 is screened entirely within the C horizon.

Within Transect 42, the timing of peak water tables within the shallow wells was often delayed from each other on the order of hours (see Figure 7) while peak water tables within deeper wells, installed in the C horizon, were delayed from those in the shallow wells on the order of days (Figure 8). In Transect 86 the timing of peak water tables within the deeper wells were only delayed by a few hours from peak water table in the shallow wells (Figure 8). Water

tables within shallow wells within each transect were flashier, responding sooner, and rising and receding at a faster rate than water tables within the C horizon (Figure 7).

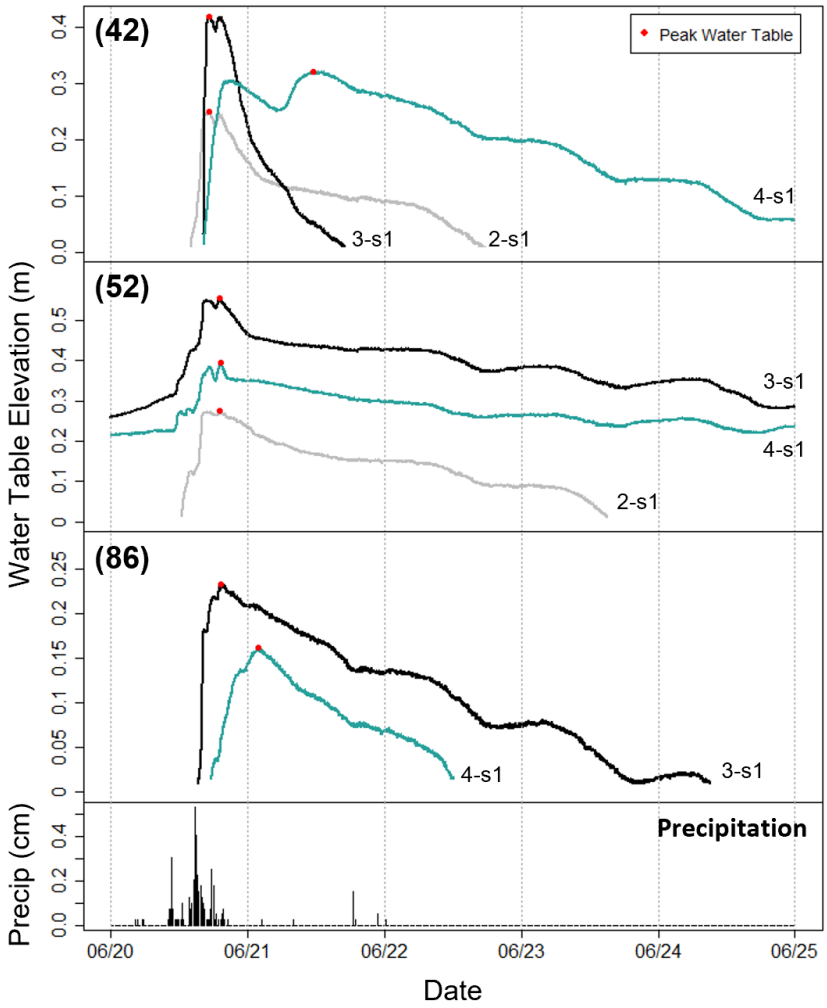

Figure 7: A time-series showing the response of water tables to a precipitation event within each transect (42, 52, & 86) at multiple hillslope positions (2-s1,3-s1, & 4-s1). Peak water table is denoted with a red circle. Hillslope position 2-s1 is the furthest upslope within each transect while hillslope position 4-s1 is furthest downslope. Water tables are expressed as elevation above the base of the solum (y = 0). See Figure 2 for transect and well locations.

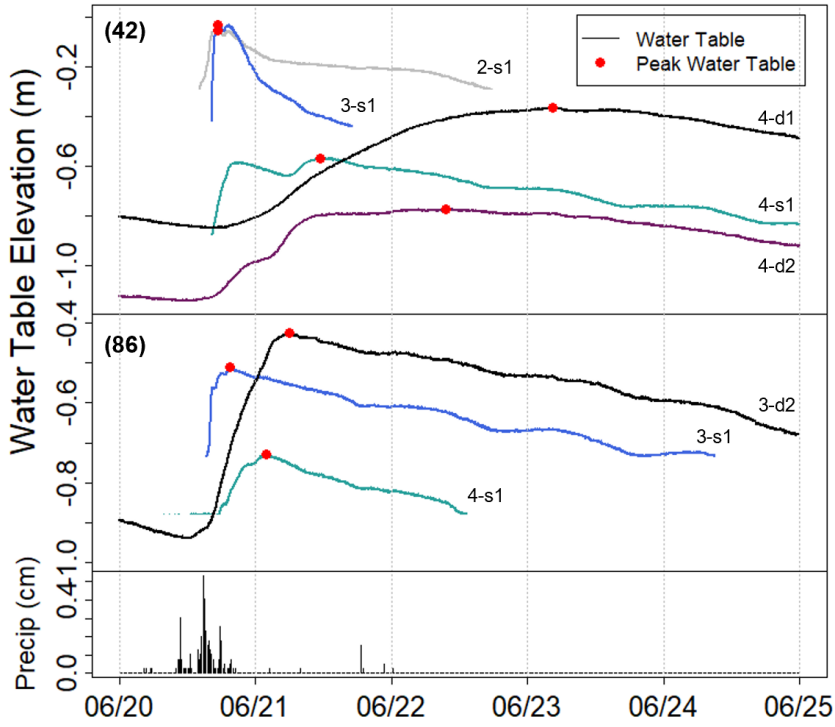

Figure 8. A time series showing water tables responding to a rain event in June, 2019 within both shallow and deep wells at Transect (42). Water tables are expressed as elevation relative to the ground surface (y = 0), and the peak water table is included to illustrate lag-times between each well (red points). See Figure 2 for transect and well locations. Well IDs 2-s1,3-s1, and 4-s1 are shallow wells and well IDs 4-d1, 4-d2, and 3-d2 are deep wells.

3.2 Saturated hydraulic conductivity

The range of saturated hydraulic conductivity (K_{sat}) values within the solum (B and E horizons) spanned two orders of magnitude with a minimum of 1.3×10^{-6} m/s, and a maximum of 1.8×10^{-4} m/s (Figure 9). The K_{sat} values measured within the C horizon were markedly lower than values measured within the solum, exhibiting a range of 5.0×10^{-8} to 1.6×10^{-6} m/s. The interquartile range of K_{sat} within the C horizon (1.5×10^{-7} to 9.8×10^{-7} m/s) is two orders of magnitude lower than the interquartile range of K_{sat} values within the B horizon (2.9×10^{-5} to 5.2×10^{-5} m/s) (Figure 9). K_{sat} measurements within the E horizon are within the range of values measured within the B horizon (Figure 9).

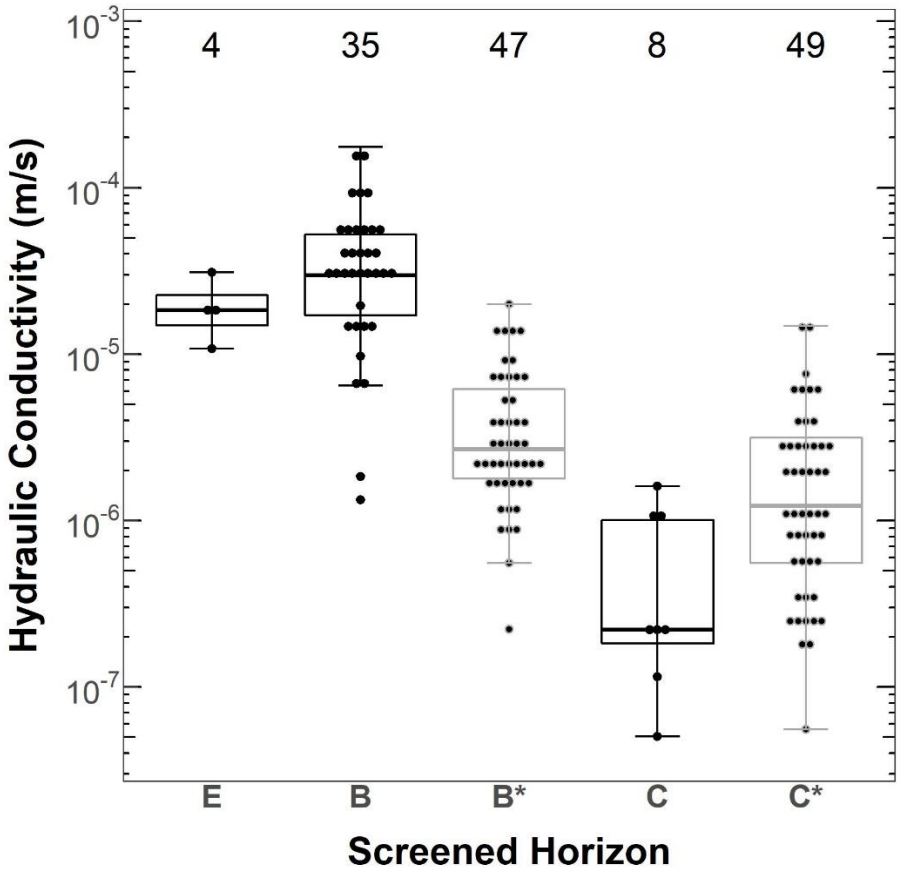

Figure 9: Box plots showing saturated hydraulic conductivity (K_{sat}) values measured within the solum comprising of wells screened within the B & E horizons, and K_{sat} values measured within the C horizon. K_{sat} values from previous work (*) using both slug test and permeameter methods are included for comparison. The number of measurements for each soil horizon is shown at the top of the boxplot.

Overall, K_{sat} within the solum is more variable than K_{sat} of the C horizon, as shown by standard deviations (SD for solum K_{sat} = 3.6 x 10^{-5} m/s is almost two orders of magnitude higher than the SD for C horizon K_{sat} = 5.9 x 10^{-7}). However, it is important to note that the number of observations within the solum (n = 39) was greater than the number of observations within the C horizon (n = 8). A one-way analysis of variance shows that K_{sat} values are significantly different between soil horizons with a p-value (0.007) less than the significance value (0.05), implying a relationship between soil horizon and K_{sat}. The comparison of K_{sat} values estimated from this study to previous studies shows that the interquartile range of values within the solum are markedly lower in previous studies, and the degree of overlap of K_{sat} between the solum and the C horizon is greater (Figure 8). Previous K_{sat} measurements shown in Figure 8 are dominantly

from borehole permeametry methods that represent smaller sample volumes and were measured primarily within the upper C horizon (Burns, 2012; Detty, 2010b). A combination of these factors may explain the differences between K_{sat} values reported in this study compared with previous studies. Regardless of these differences, previous studies support results of this study that show an overall decrease in both the median and interquartile range of K_{sat} values between the solum and the C horizon (Figure 8).

3.3 Groundwater flow direction, surface topography, and the C horizon

Throughout the study period, the mean groundwater flow direction followed the large-scale slope direction of surface topography within WS3 (SE or SW; Table 3). The mean slope direction of the ground surface for well clusters on the southeast facing slope was 144 degrees azimuth and the mean flow direction was 150 degrees azimuth. The average surface slope direction for well clusters on the southwest facing slope was 244 degrees and the mean flow direction was 247 degrees azimuth. However, under certain conditions, flow direction showed deviations from the surface topography by as much as 56 degrees, with a maximum range of 61 degrees, and a minimum range of 10 degrees (Table 3).

Table 3: Summary statistics for groundwater flow direction for each well cluster in W3, the number of measurements (n), and the maximum slope direction for the top of the C horizon and the ground surface at each well cluster location. The directional units (azimuth) are reported in degrees from North. See Figure 2 for cluster locations.

	Groundwater Flow Direction (azimuth)							Azimuth	
Cluster	Minimum	Maximum	Mean	Standard Deviation	25th Percentile	75th Percentile	n	Ground Surface	C Horizon
42-3-c1	134.63	151.99	140.71	2.14	139.25	142.04	**12312**	138.76	139.49
42-4-c1	157.02	173.14	166.50	2.00	165.31	167.38	**56072**	160.84	159.34
52-4-c1	127.62	188.68	142.97	6.05	139.72	146.28	**90576**	132.83	150.19
86-4-c1	229.03	257.43	246.08	5.29	242.99	250.48	**7906**	242.16	255.01
86-3-c1	243.50	252.73	247.68	1.76	246.36	248.86	**30921**	245.67	250.88

Within all well clusters, the direction of groundwater flow mimicked surface topography during higher water tables and deviated from surface topography during lower water tables. Three examples are used to show these patterns (Figures 10-12). The first example is a well cluster (4c-1) from transect 52 (Figure 10). During higher water table regimes, both the hydraulic gradient and direction of flow were closer to the surface topography (Figure 10A, B). However, under lower water table regimes, the flow direction deviated from surface topography towards the slope direction of the top of the C horizon (Figure 10A, B). Flow directions calculated over time had a normal distribution with an arithmetic mean between the surface topography and the C horizon slope direction (Figure 10C).

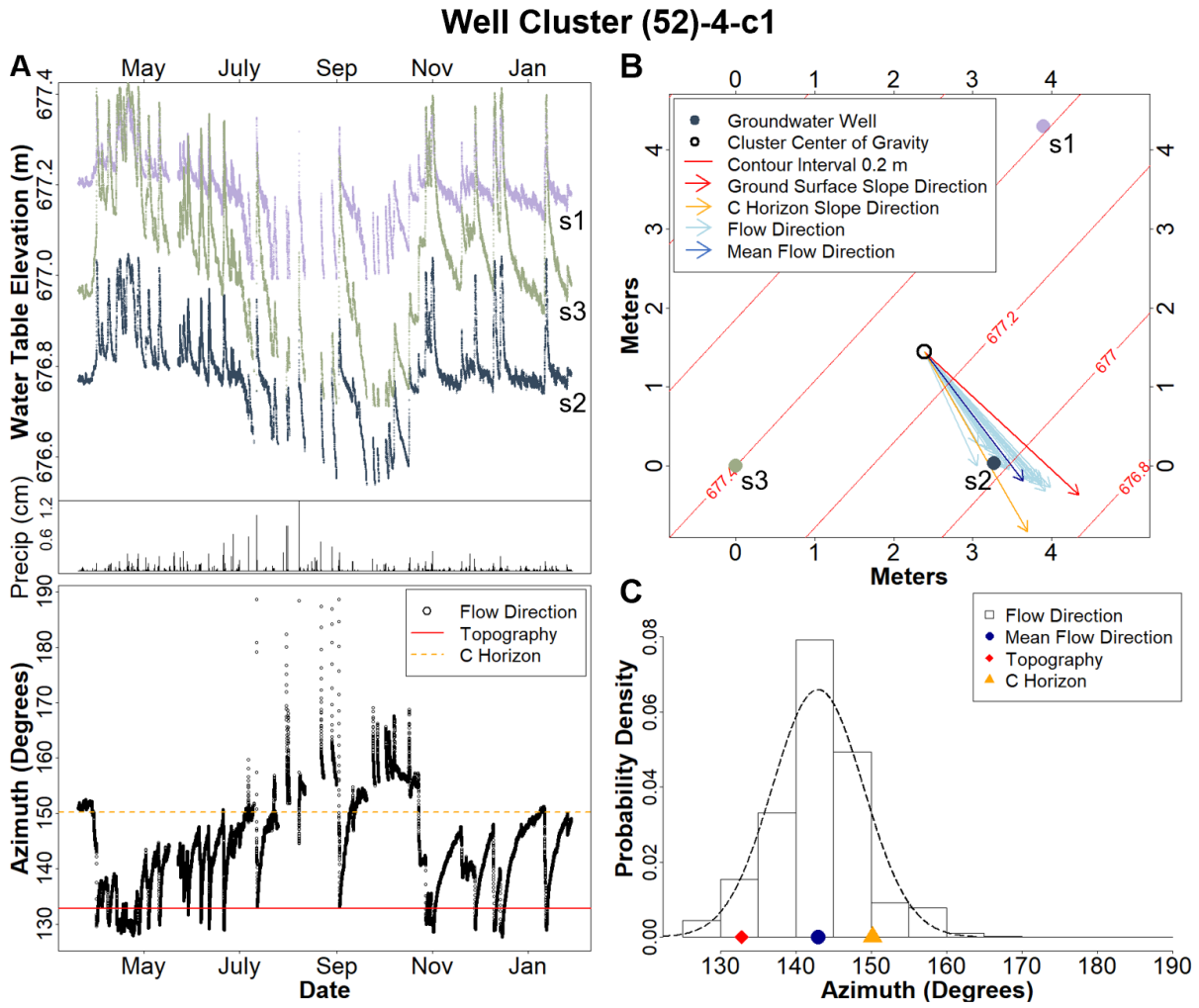

Figure 10.A: A time series showing water table elevation, precipitation, and groundwater flow direction for a well cluster. Missing data within the time-series reflects the lack of sufficient water levels (in all three wells) needed for gradient calculations 4.B: A map view of the well

cluster showing the variability in groundwater flow direction (blue vectors) in relation to the slope direction of the ground surface (red vectors) and the top of the C horizon (yellow vectors). The magnitude (length) of each vector is scaled proportional to the horizontal hydraulic gradient. 4.C: A probability density histogram summarizing groundwater flow direction with the slope direction of surface topography and the top of the C horizon. The dashed line is the normal distribution corresponding to the sample mean and standard deviation (Table 3).

In the second example from transect 86, flow direction within well cluster 3-c1 showed similar trends as 52-4-c1 in following surface topography under higher water tables, the top of the C horizon under lower water tables, and an arithmetic mean between the C horizon and the surface topography (Figure 11). Similar to the first example, the interquartile range (Table 3) and highest probability of flow direction (Figure 11C) falls between the slope direction of the top of the C horizon and the ground surface, and these features constrain the range in flow direction observed at each well cluster (Figures 10-11).

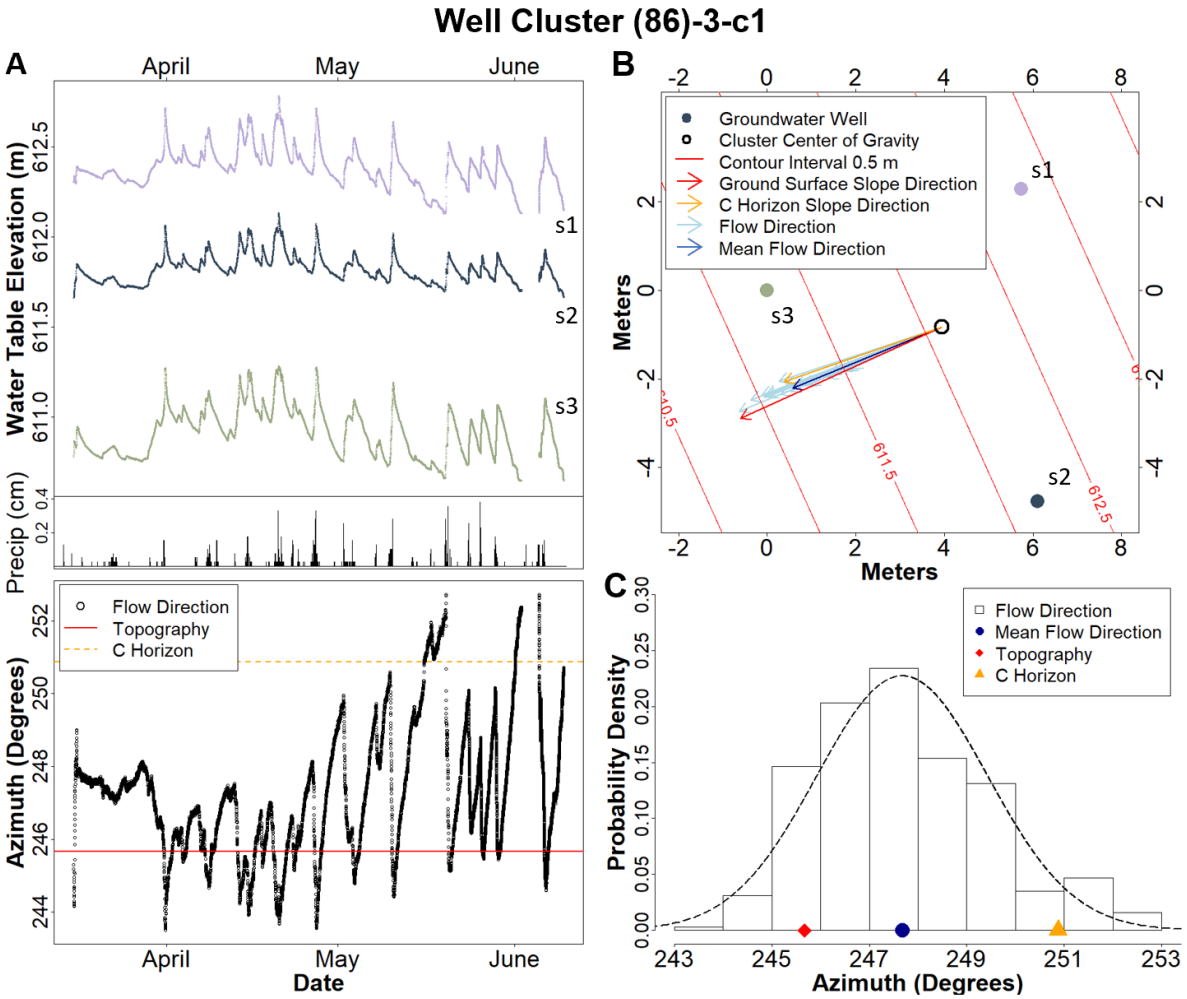

Figure 11: A time series showing water table elevation, precipitation, and groundwater flow direction for a well cluster. Missing data within the time-series reflects the lack of sufficient water levels (in all three wells) needed for gradient calculations 4.B: A map view of the well cluster showing the variability in groundwater flow direction (blue vectors) in relation to the slope direction of the ground surface (red vectors) and the top of the C horizon (yellow vectors). The magnitude (length) of each vector is scaled proportional to the horizontal hydraulic gradient. 4.C: A probability density histogram summarizing groundwater flow direction with the slope direction of surface topography and the top of the C horizon. The dashed line is the normal distribution corresponding to the sample mean and standard deviation (Table 3).

In the third example from transect 41, flow direction within well cluster 4-c1 followed surface topography under higher water tables; however, it deviated from both the surface topography and the top of the C horizon under lower water tables (Figure 12). The highest probability of flow direction occuring at the mean (Figure 12C) was offset from the ground surface by 6 degrees azimuth, and the slope direction of the ground surface is approximately equal to the slope direction of the surface of the C horizon (Figure 12C).

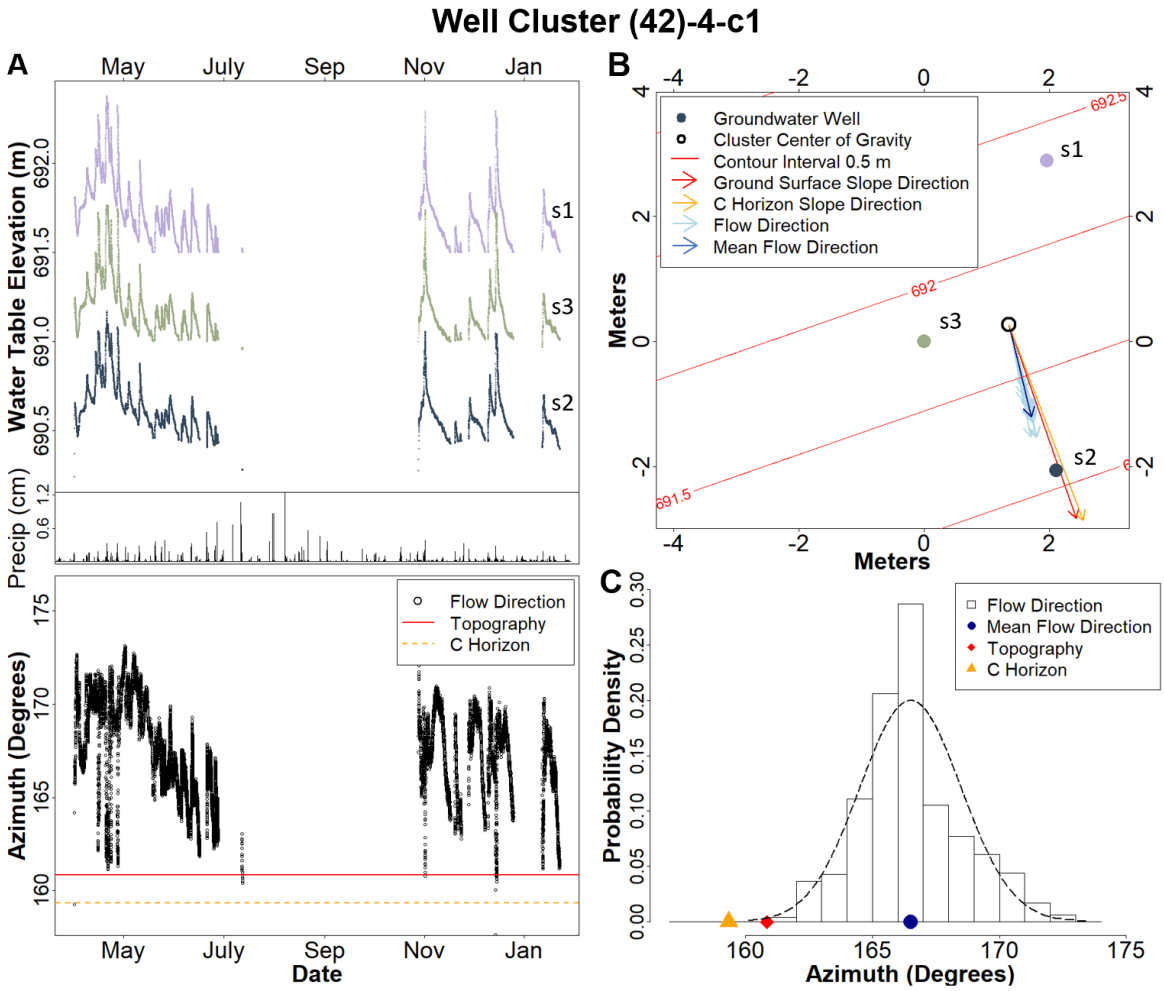

Figure 12: A time series showing water table elevation, precipitation, and groundwater flow direction for a well cluster. Missing data within the time-series reflects the lack of sufficient water levels (in all three wells) needed for gradient calculations 4.B: A map view of the well cluster showing the variability in groundwater flow direction (blue vectors) in relation to the slope direction of the ground surface (red vectors) and the top of the C horizon (yellow vectors). The magnitude (length) of each vector is scaled proportional to the horizontal hydraulic gradient. 4.C: A probability density histogram summarizing groundwater flow direction with the slope direction of surface topography and the top of the C horizon. The dashed line is the normal distribution corresponding to the sample mean and standard deviation (Table 3).

The relationship between flow direction, surface topography, and the top of the C horizon is highlighted when the time series of water table fluctuations and flow direction are examined at a finer temporal scale in transect 86. Figure 13 shows the response of water tables in well cluster (86)-3-c1 immediately following a storm event, and the associated flow direction calculations. At the beginning of the event (t_0) whenever water levels are lower, closer to the base of the well, the

flow direction mimics the top of the C horizon (Figure 12), and this trend continues until water levels begin to increase (t_1) in response to a precipitation event. As the water table increases, flow direction deviates in the southward direction. As water tables peak (t_2) at approximately at 8 hours after t_1, flow direction is within a degree of the surface topography.

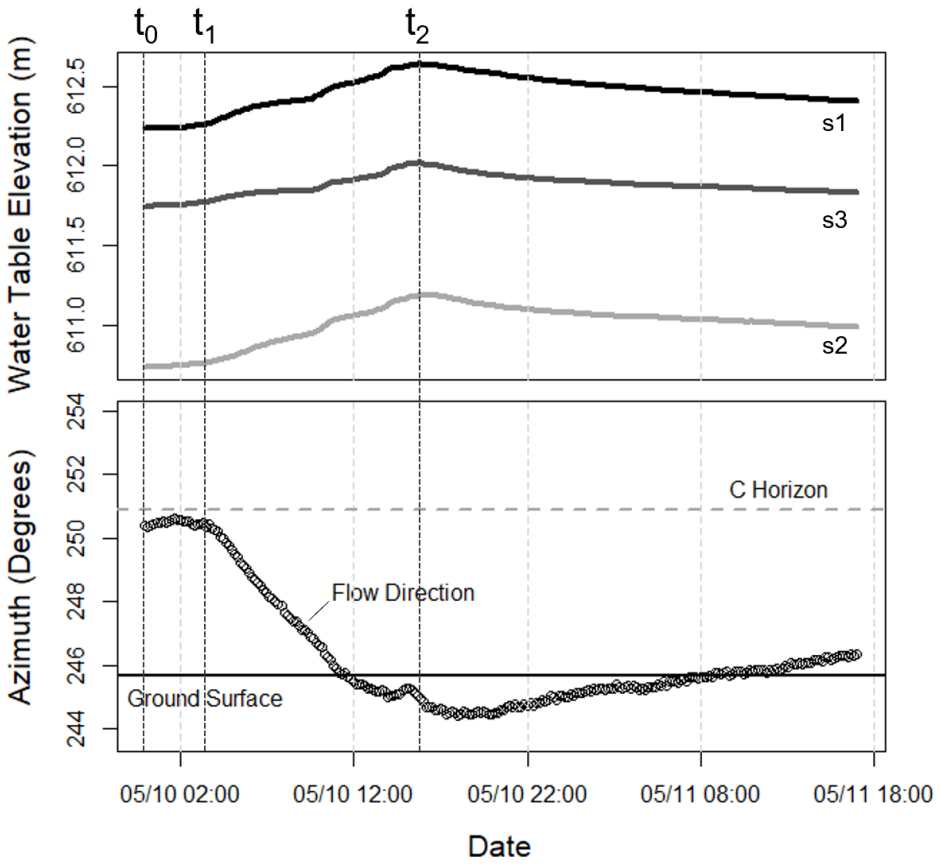

Figure 13: A time-series of water levels responding to a precipitation event in early May 2019 with the calculated flow direction at 10-minute intervals. The beginning of the event (t_0), time of water table response (t_1), and the peak water table (t_2) are marked by dashed vertical lines. The slope direction of the ground surface and top of the C horizon is also included for comparison. Water tables are expressed in elevation relative to mean sea level.

3.4 Hydraulic gradient and hydrologic fluxes

The magnitude of the hydraulic gradient and subsurface hydrologic fluxes (assuming a constant K_{sat}) varied with respect to changing water table elevations (Figure 14). Within some well clusters, hydraulic gradient and hydrologic fluxes decreased with decreasing water table

elevations (42-4-c1 and 52-4-c1, Figure 14) while other well clusters exhibited an inverse relationship (42-3-c1 and 86-3-c1, Figure 14) with an increase in gradient magnitude and flux with decreasing water table elevation.

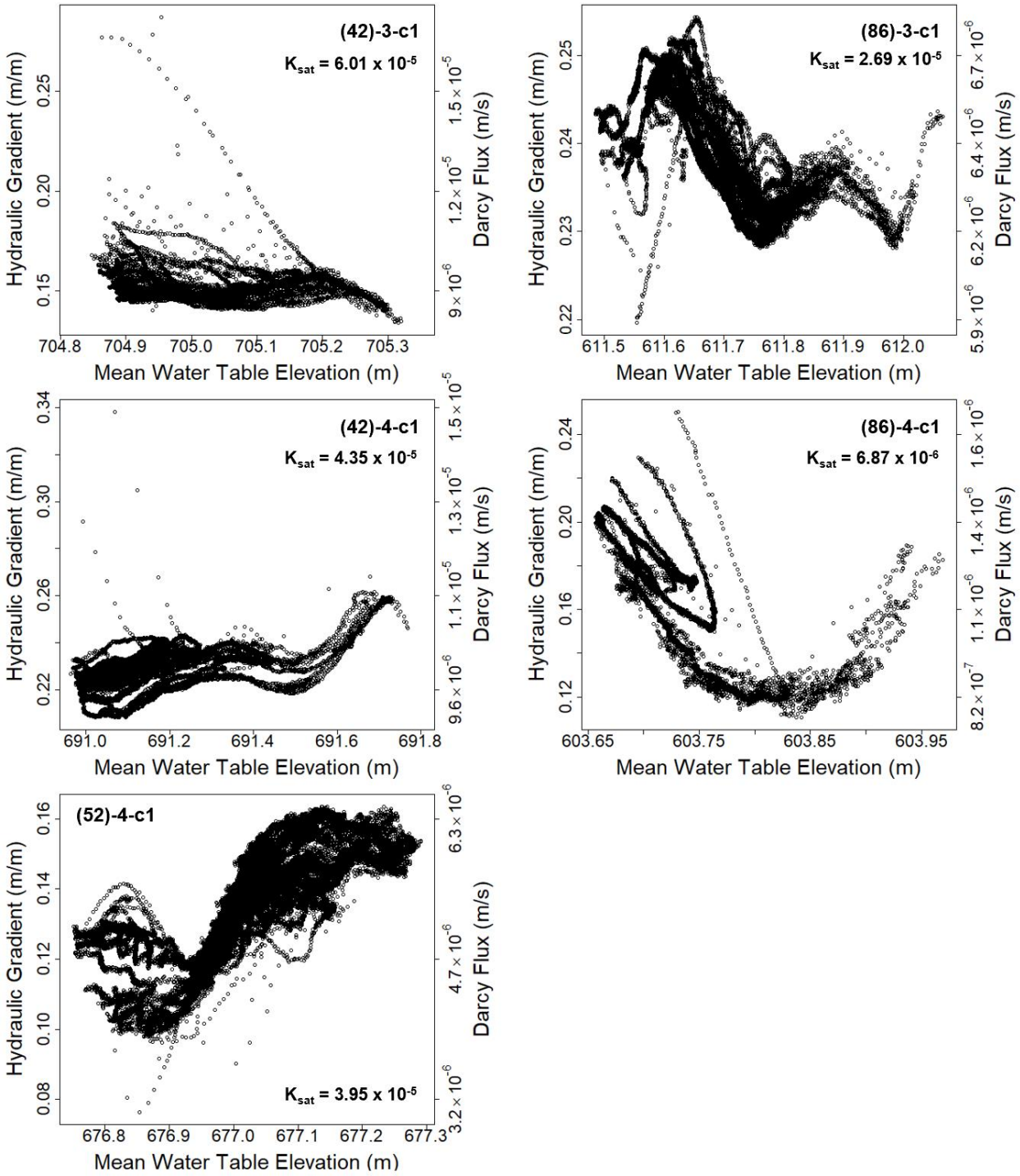

Figure 14: The magnitude of hydraulic gradient (Equation 4), and hydrologic flux (Darcy Flux, Equation 5) plotted against mean water table elevation; and the mean saturated hydraulic conductivity (K_{sat}) used for hydrologic flux calculations is shown for each well cluster.

The well cluster that exhibited the largest range in flow direction, (52)-4-c1, also exhibited the second-to-largest range in gradient magnitude and flux (0.08 to 0.16 m/m, 3.01 x 10^{-6} to 6.45 x 10^{-6} m/s, respectively) with the lowest values occurring during lower water table regimes and higher values during higher water table regimes (Figure 14). In contrast, well cluster (86)-4-c1, showed a different relationship, in which gradient magnitude and flux generally increased with decreasing water table elevation (Figure 14) below a threshold of around 603.85 m AMSL; above that level, gradient magnitude and fluxes increased.

3.5 Deviations in subsurface topography from surface topography

The difference between the slope direction of the ground surface and the top of the C horizon (ΔGC) determined from the auger investigation in each subcatchment varied between transects. Three examples are included (Figures 15-17) to illustrate ΔGC patterns across WS3. ΔGC measurements from each well cluster are also included for comparison. Overall, ΔGC had a larger range (± 30 degrees) of values compared to the ΔGC variability observed within the well clusters; however, the highest frequency of ΔGC observations from auger investigations showed similar trends to ΔGC observed at each well cluster (Figures 15-17). For example, the highest frequency of ΔGC measurements within transect 42 ranged between ± 10 degrees within a slightly positive skew and ΔGC observed within the well clusters also ranged between ± 10 degrees (Figure 15). In transect 86, the majority of ΔGC measurements were negative, and both ΔGC measurements within the well clusters are also negative (Figure 16). Finally, in transect 52, ΔGC measured at the well cluster coincided with the larger frequency of ΔGC values derived from the auger investigation (Figure 17).

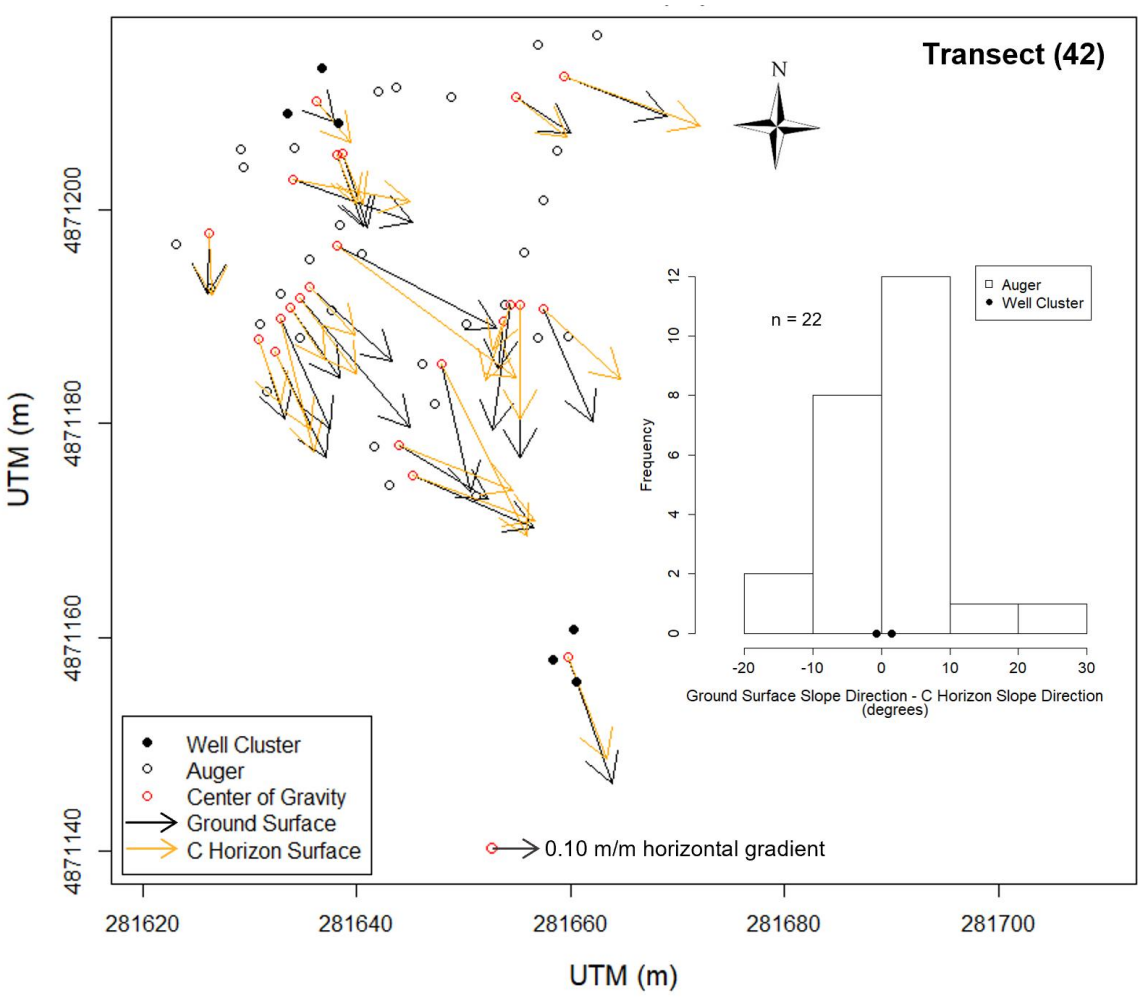

Figure 15: A map showing the location of auger investigations, shallow wells, and surface slope directions derived from three-point gradient calculations. Slope directions are illustrated by vectors originating from the centroid of each three-point cluster where the directional component of vectors is opposite to the direction of maximum horizontal gradient (downslope) and the magnitude of vectors are scaled proportional to the maximum horizontal gradient. A frequency histogram is included summarizing the difference in slope direction between the ground surface and the top of the C horizon. Measurements from well clusters are included for comparison.

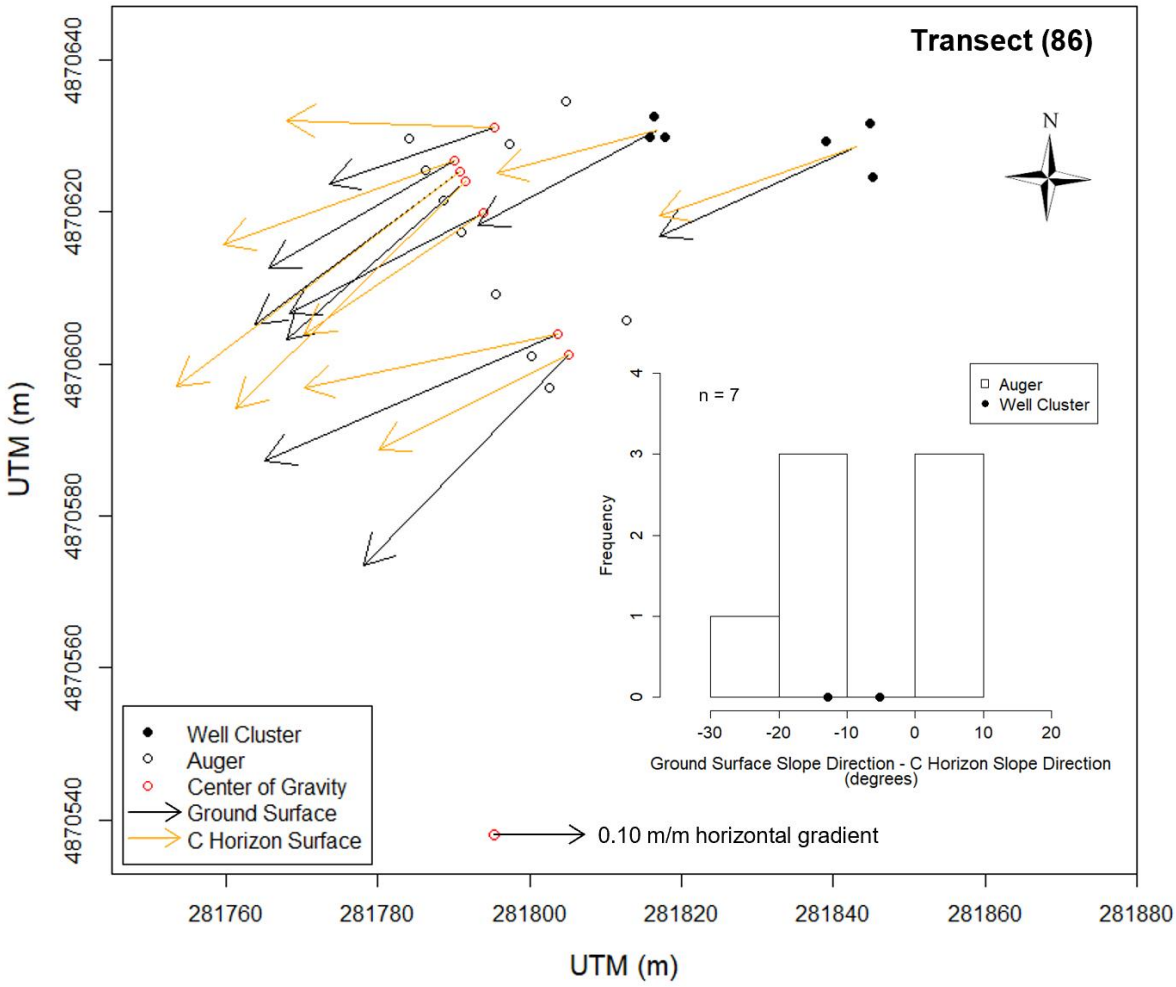

Figure 16: A map showing the location of auger investigations, shallow wells, and surface slope directions derived from three-point gradient calculations. Slope directions are illustrated by vectors originating from the centroid of each three-point cluster where the directional component of vectors is opposite to the direction of maximum horizontal gradient (downslope) and the magnitude of vectors are scaled proportional to the maximum horizontal gradient. A frequency histogram is included summarizing the difference in slope direction between the ground surface and the top of the C horizon. Measurements from well clusters are included for comparison.

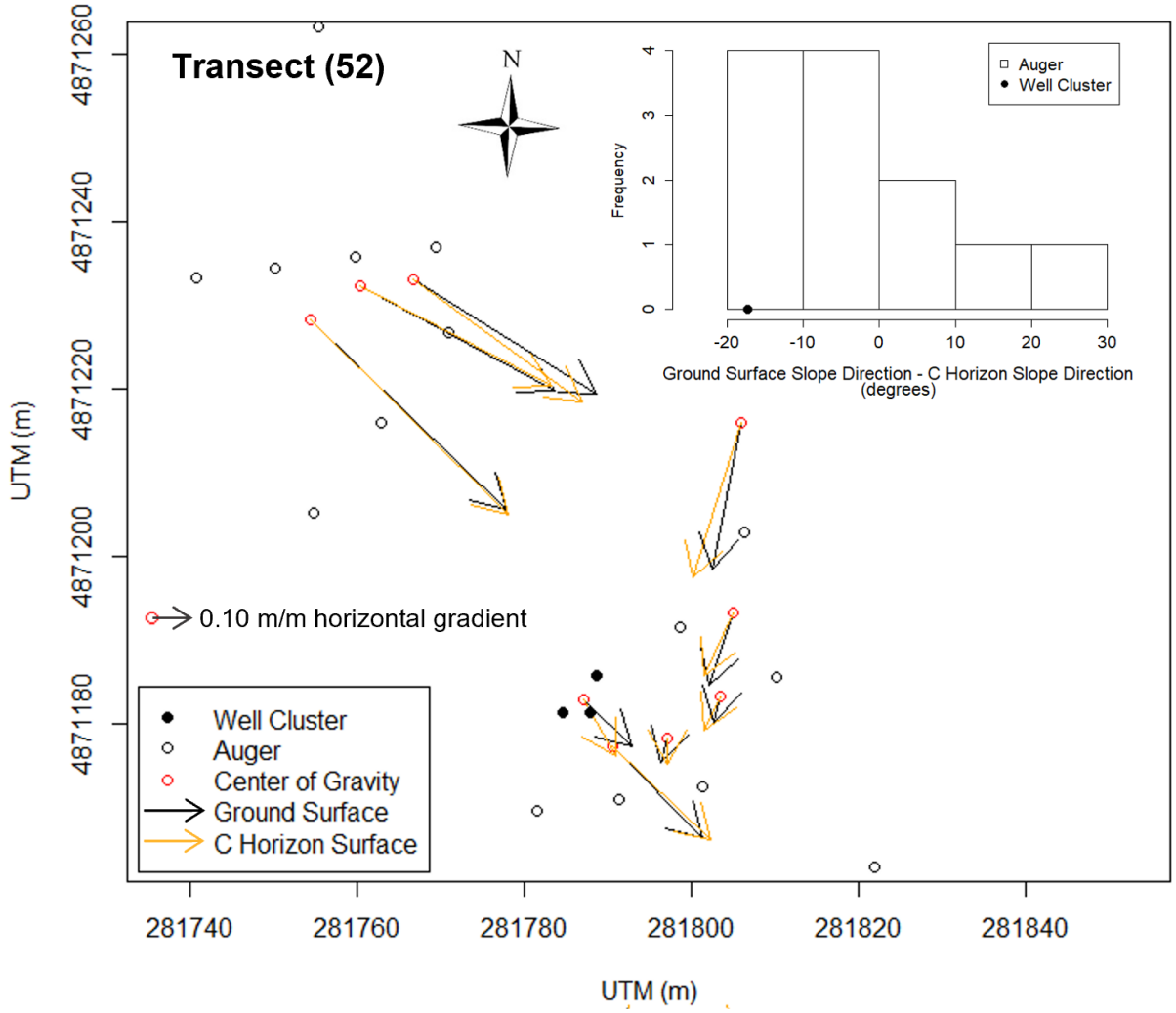

Figure 17: A map showing the location of auger investigations, shallow wells, and surface slope directions derived from three-point gradient calculations in Transect (52). Slope directions are illustrated by vectors originating from the centroid of each three-point cluster where the directional component of vectors is opposite to the direction of maximum horizontal gradient (downslope) and the magnitude of vectors are scaled proportional to the maximum horizontal gradient. A frequency histogram is included summarizing the difference in slope direction between the ground surface and the top of the C horizon. Measurements from well clusters are included for comparison.

4.0 Discussion

4.1 Groundwater flow variability

Shallow groundwater flow in this glaciated headwater catchment exhibits substantial variations in both flow direction and magnitude. The total range of groundwater flow direction over the monitoring period within the solum was greater than 60 degrees in some locations (Table 2) but was less than 10 degrees in other locations. The magnitude of hydraulic gradient doubled with respect to changing water table elevation within some locations but varied less within others (Figure 14). The shifts in flow direction occurred over short time scales (hours to days) on an event basis (Figure 13) and also exhibited longer time-scale seasonal patterns as water table elevations decrease during the summer months and rise during the fall, winter, and spring months (Figure 10). Both short-term and seasonal patterns in flow direction show that groundwater flow direction varies in response to changing water table elevation (Figures 10-13) and highlights the presence of non-uniform response of water tables in WS3.

Results from this study show considerably more variability in groundwater flow direction within the upper hillslopes of WS3 than in the upper hillslopes of headwater catchments reported in other studies (Rhode et al. 2011, von Freyberg et al. 2014). This difference may be due to prior research investigating groundwater flow direction in headwater catchments has primarily focused on characterizing hillslope-streamflow connectivity (Tromp-van Meerveld et al. 2015, Vidon and Smith, 2007) with the majority of observations constrained to the lower hillslopes and riparian zones, and considerably fewer observations in the upper hillslopes. Groundwater flow within the riparian zone is heavily influenced by streamflow by directing subsurface flow in response to stream stage (Rhode et al. 2011, Vidon and Smith, 2007) that may override the effect that permeability contrasts on flow direction (the focus of this study). However, results from this study show that groundwater flow direction is more variable in the upper hillslopes of a glaciated, headwater catchment than previous work may imply.

4.2 Implications for using surface topography as an approximation for hydraulic gradients

Due to the availability of land surface DEM data, It is common practice within modeling-based hydrologic studies in headwater catchments to use the land surface as an approximation of

hydraulic gradient magnitude (Nippgen et al., 2015, Beven, 1997, Wigmosta et al. 1994). A widely used topographically driven rainfall-runoff model, TOPMODEL (Beven and Kirkby 1979, Beven, 1997), uses the slope of the land surface to calculate topographic wetness indices as a steady-state approximation of groundwater dynamics at each point within the catchment. Another widely used rainfall-runoff model, the distributed hydrologic vegetation model (Wigmosta et al. 1994) approximates subsurface hydrologic gradients with land surface topographic gradients and thus routes subsurface water according to the surface topography. Previous experimental (field-based) investigations at WS3 have also used surface topographic gradients surrounding a single well as an approximation for subsurface hydraulic gradients in soils to investigate the response of subsurface fluxes to catchment storage dynamics (Detty and McGuire 2010a, Gannon et al. 2014).

In this study, we observe dynamic changes in the magnitude of hydraulic gradients in response to changing water table elevation (Figure 14). Within some locations, the magnitude of the hydraulic gradient, and subsequently, the hydrologic flux, decreases as water table elevation decreases (52-4-c1 & 42-4-c1, Figure 14), suggesting that using surface topography as an approximation for water table gradients at these locations would produce an over-estimation of subsurface hydrologic fluxes during dry periods. In contrast, at some other locations, the magnitude of the hydraulic gradient and hydrologic flux increase with decreasing water table elevations (Figure 14, 86-4-c1) below a threshold; above the threshold, the patterns show increases in gradient/flux with water table. Overall, the results show that the magnitude of the hydraulic gradient can deviate from the maximum slope of the land surface (Table 1) by as much as 0.11 m/m. Thus, the assumption that the hydraulic gradient can be approximated by surface topography may be invalid. Results of study highlight the need for the characterization and establishment of a functional relationship between water table elevation and hydraulic gradients within the solum to provide a more accurate estimation of the temporal dynamics of hydrologic fluxes that otherwise may produce significant error in predicting runoff-rainfall response through hydrologic modeling.

4.3 Relationships between flow direction, water table elevation, surface topography, and subsurface topography

Results from this study are consistent with results from Tromp-van Meerveld et al. (2015) and Hutchinson and Moore (2000) in that groundwater flow direction correlates with subsurface topography of confining units during lower water tables but follows surface topography during higher water tables (Figure 14). For most locations within this study, the mean and interquartile range of flow direction observations were confined between the slope direction of the land surface and the slope direction of the C horizon (Table 3, Figures 10-11). Tromp-van Meerveld et al. (2015) observed the largest standard deviation in hillslope flow directions within well clusters located in a bedrock hollow where the bedrock surface deviated from surface contours, and smaller deviation in hillslope flow directions where the bedrock surface followed surface topography. Similarly, the largest standard deviation in flow direction measured in this study, 52-4-c1, coincided with the largest difference in slope direction of C horizon topography from surface topography (Table 3). These results imply the top of the C horizon and the land surface may act as end members defining the upper and lower bounds of flow direction variability within locations where the C horizon is a confining unit relative to the solum. Therefore, knowledge of C horizon topography may provide a constraint for characterizing the heterogeneity of event-based throughflow in soils at WS3.

Results from our catchment-scale auger investigation shows that the deviation of subsurface topography from surface topography observed at each well cluster can be generalized, and falls within a range of deviations observed at the larger scale (Figures 15-17), decreasing the likelihood that subsurface deviations observed at each well cluster is entirely localized. Therefore, variability in flow direction may also be generalized at the hillslope scale using methods presented within this study; assuming that permeability contrasts are continuous.

4.4 Heterogeneity in permeability contrasts

Permeability contrasts between soils and underlying parent materials influence the distribution of energy potentials (the ultimate force that determines the direction of water flow). The C horizon in WS3 has a statistically significantly lower permeability (measured as hydraulic conductivity) than the solum (Figure 9), however, the C horizon is texturally heterogenous, and

can have zones of higher permeability (Bailey et al. 2014) due to the presence of sand lenses that, if present, may not result in a decrease in permeability at the interface between the solum and C horizon. Additionally, the interface between the C horizon and the solum can be gradual and will not necessarily correspond to abrupt changes in hydraulic properties. Results from this study, combined with hydraulic conductivity estimates from previous work, add to the total range of possible K_{sat} values for both the solum and the C horizon, therefore increasing the possible range of permeability contrasts between soils and the underlying parent material in WS3. This spatial heterogeneity in the hydraulic properties of glacial sediments comprising both the C horizon and solum makes it difficult to generalize hydraulic behavior observed at the smaller, subcatchment scale for the entire catchment of WS3. Additionally, this heterogeneity may explain why the deviation in flow direction at some locations in this study do not correlate with C horizon topography (Figure 12).

4.5 Throughflow generation: perched saturation versus transmissivity feedback

Results of this study do not resolve if throughflow within the solum at WS3 is perched on top of the C horizon or an expression of deeper water tables rising from beneath, or if it reflects a combination of both depending upon location specific hydraulic properties (permeability contrasts) and time-variable conditions such as rainfall intensity. If there is a permeability contrast between the C horizon and the solum, both mechanisms of throughflow (transmissivity feedback and perched saturation) could theoretically result in a water table configuration that mimics the top of the C horizon so flow direction dynamics may not have direct implications towards the presence (or lack thereof) of perched saturation. Previous work in characterizing soil moisture response to precipitation events in WS3 shows that soil moisture within the solum can be much more temporally dynamic (Detty and McGuire, 2010b) and responsive to rain events compared to soil moisture observed within the upper C horizon (measured a few centimeters below the solum), implying that perched saturation may be occurring at the base of the solum in specific locations. Results from this study show that peak water table occurrence within the middle to lower parts (2.4 to 6.9 m depth) of the C horizon is consistently delayed relative to peak water table occurrence in the solum, regardless of landscape position (Figure 8), and water tables within the C horizon are not as responsive (flashy) as water table response within the solum (Figure 6). The presence of peak-lag times combined with the temporal behavior of water

tables within the C horizon could be interpreted to reflect a distinct hydrologic system that is separated from saturation observed within the solum. Although results from this work cannot identify the dominance of one runoff generation mechanism versus another for WS3, results are suggestive that throughflow development may be influenced by both shallow perched saturation and deeper flow systems, depending upon infiltration conditions, recharge intensity, permeability contrasts, and antecedent moisture conditions that are not generalizable for the entire catchment. Further work is needed on this topic.

4.6 Conceptual model

Based on the results of this work, I present a simple conceptual model (Figure 18) for groundwater flow direction within the solum changing in response to rising water table conditions immediately following a recharge event. This conceptual model assumes that a permeability contrast is present at the interface between the solum and the C horizon and applies to 1.) water tables rising from the deeper groundwater system into the solum or 2.) perched saturation developing within the upper C horizon rising into the solum. In scenario 1, at an early time-step immediately following a precipitation event ($\mathbf{t_1}$) saturation rises from the deeper groundwater flow system into the solum. The higher transmissivity of the solum increases the lateral flux of water moving downslope (transmissivity feedback), therefore decreasing the rate of water table rise above the interface between the solum and C horizon. This leads to water table configurations mimicking the topography of the C horizon. In scenario 2, at $\mathbf{t_1}$ perched saturation develops at the base of the solum directly above the impeding C horizon, causing water tables to mimic the C horizon. Applicable to both scenarios, as conditions continue to wet up, water tables connect spatially across the landscape and flow direction shifts towards the direction of the land surface ($\mathbf{t_2}$) implying an increase in hydraulic connectivity between saturated zones (Ambroise, 2004, Tromp-van Meerveld and McDonnell, 2006, Detty and McGuire 2010b).

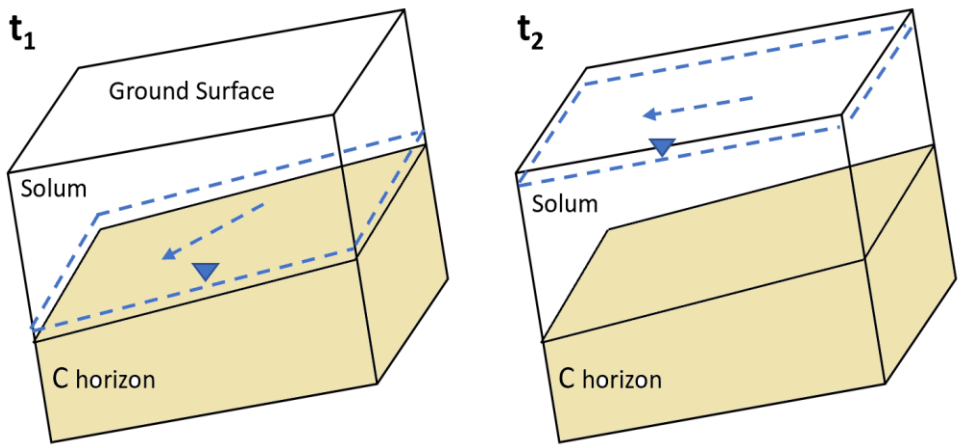

Figure 28: A conceptual model showing the development of perched saturation on top of a C horizon surface that slopes away from surface topography. The dashed blue line represents the water table while the dashed blue arrow represents the direction of flow.

4.7 Study limitations

One limitation of this study is the use of the three-point method to determine hydraulic gradients. This method assumes that groundwater flows through a homogenous, isotropic porous medium and ignores preferential flow paths through macropores that are ubiquitous in forest soils. The presence of animal burrow holes and root channels (bioturbation), and soil erosion features are common within the soil zone that can lead to rapid turbulent flow in the subsurface that may be in a direction different from what is predicted by Darcian assumptions. Macropore features were not identified or characterized in this study, and as a result this portion of groundwater flow was ignored. Additionally, flow through macropores affects the saturated hydraulic conductivity of soils, which is ignored using the Hvorslev slug test method that also assumes laminar flow through homogenous, isotropic materials. All these assumptions of Darcian flow may lead to error in estimating groundwater flow paths and fluxes. The degree of this error depends upon how large of a portion preferential flow constitutes of total subsurface flow.

Another limitation of this study is the spatial coverage of water-table observations and hydraulic gradient measurements. Hydraulic gradient measurements were limited to 5 locations, and therefore interpretations of the factors influencing groundwater flow variability were also

limited, and difficult to scale up or generalize due to the heterogeneity of the glacial till present at the study site.

5.0 Conclusions

In this study I observed the temporal behavior of groundwater flow direction within soils at five different hillslope positions in a glaciated headwater catchment (WS3) at the Hubbard Brook Experimental Forest. Through high frequency water table measurements collected across a ten-month period, I determined that groundwater flow direction changes over short time scales, but also exhibited long term patterns. The results from this study show that groundwater flow direction can be highly variable within the upper hillslopes of a steep headwater glaciated catchment where subsurface gradients are often assumed to follow surface topography. I show that variability in flow direction is controlled by both surface topography and the subsurface topography of confining units (C horizon) such that during wet conditions, groundwater flow direction follows surface topography while under dry conditions, groundwater flow direction dominantly follows subsurface topography. Additionally, I show that deviations in groundwater flow direction may be generalizable at the hillslope scale if soil unit depths and thicknesses are measured. However, hydraulic properties of the solum and C horizon are also spatially heterogenous making it difficult to generalize groundwater flow conditions observed at a specific hillslope for the entire catchment (WS3). In conclusion, knowledge of the topography (thickness and elevation) of subsurface soil units, especially confining units, and the spatiotemporal patterns of water table dynamics can constrain estimates of the magnitude and direction of shallow groundwater flow in headwater catchments. This information, in turn, can be applied to enhancing our ability to estimate subsurface hydrologic fluxes in response to hydrologic events such as rain and snowmelt.

References

Alexander, R. B., Boyer, E. W., Smith, R. A., Schwarz, G. E., & Moore, R. B. (2007). The role of headwater streams in downstream water quality. *Journal of the American Water Resources Association*, *43*(1), 41–59. https://doi.org/10.1111/j.1752-1688.2007.00005.x

Alexander, L. C., Fritz, K. M., Schofield, K. A., Autrey, B. C., DeMeester, J. E., Golden, H. E., … Wigington, P. J. (2018). Featured Collection Introduction: Connectivity of Streams and Wetlands to Downstream Waters. *Journal of the American Water Resources Association*, *54*(2), 287–297. https://doi.org/10.1111/1752-1688.12630

Ambroise, B. (2004). Variable ‘active’versus ‘contributing’areas or periods: a necessary distinction. *Hydrological Processes*, *18*(6), 1149-1155.

Bailey, A. S., J. W. Hornbeck, J. L. Campbell and C. Eagar. 2003. Hydrometeorological database for Hubbard Brook Experimental Forest: 1955-2000. General Technical Report NE-305. U.S. Department of Agriculture, Forest Service, Northeastern Research Station, Newtown Square, PA. 36 p.

Bailey, S. W., Brousseau, P. A., McGuire, K. J., & Ross, D. S. (2014). Influence of landscape position and transient water table on soil development and carbon distribution in a steep, headwater catchment. *Geoderma*, *226–227*(1), 279–289. https://doi.org/10.1016/j.geoderma.2014.02.017

Bailey, S. W., McGuire, K. J., Ross, D. S., Green, M. B., & Fraser, O. L. (2019). Mineral weathering and podzolization control acid neutralization and streamwater chemistry gradients in upland glaciated catchments, Northeastern United States. *Frontiers in Earth Science*, *7*(April), 1–18. https://doi.org/10.3389/feart.2019.00063

Beven, K.J. and Kirkby, M.J. (1979) A Physically Based, Variable Contributing Area Model of Basin Hydrology. Un modèle à base physique de zone d'appel variable de l'hydrologie du bassin versant. Hydrological Sciences Bulletin, 24, 43-69. http://dx.doi.org/10.1080/02626667909491834

Beven, K. (1997). TOPMODEL : A CRITIQUE. *Hydrological Processes*, *11*.

Bormann, F.H., Likens, G. E. (1965). Small watersheds can provide invaluable information about terrestrial ecosystems., *155*, 1965.

Burns, M. A. (2012). The Hydrological and Geochemical Role of the C Horizon in a Glacial Till Mantled Headwater Catchment.

Carroll, R. W. H., Deems, J. S., Niswonger, R., Schumer, R., & Williams, K. H. (2019). The Importance of Interflow to Groundwater Recharge in a Snowmelt-Dominated Headwater Basin. *Geophysical Research Letters*, *46*(11), 5899–5908. https://doi.org/10.1029/2019GL082447

Chifflard, P., Blume, T., Maerker, K., Hopp, L., van Meerveld, I., Graef, T., … Achleitner, S. (2019). How can we model subsurface stormflow at the catchment scale if we cannot measure it? *Hydrological Processes*, *33*(9), 1378–1385. https://doi.org/10.1002/hyp.13407

Clarke, A., Mac Nally, R., Bond, N., & Lake, P. S. (2008). Macroinvertebrate diversity in headwater streams: A review. *Freshwater Biology*, *53*(9), 1707–1721. https://doi.org/10.1111/j.1365-2427.2008.02041.x

Darcy, H. (1856). Les fontaines publiques de la ville de Dijon : exposition et application des principes à suivre et des formules à [...].

Datry, T., Larned, S. T., & Tockner, K. (2014). Intermittent rivers: a challenge for freshwater ecology. BioScience, 64(3), 229–235.

Detty, J. M., & McGuire, K. J. (2010a). Threshold changes in storm runoff generation at a till-mantled headwater catchment. *Water Resources Research*, *46*(7), 1–15. https://doi.org/10.1029/2009WR008102

Detty, J. M., & McGuire, K. J. (2010b). Topographic controls on shallow groundwater dynamics: Implications of hydrologic connectivity between hillslopes and riparian zones in a till mantled catchment. *Hydrological Processes*, *24*(16), 2222–2236. https://doi.org/10.1002/hyp.7656

Dunlap, L. E., & Spinazola, J. M. (1984). Interpolating water-table altitudes in west-central Kansas using kriging techniques (Ogallala aquifer). *US Geological Survey Water-Supply Paper*, *2238*(1). https://doi.org/10.3133/ofr811062

Gannon, J. P., Bailey, S. W., & McGuire, K. J. (2014). Organizing groundwater regimes and response thresholds by soils: A framework for understanding runoff generation in a headwater catchment. *Water Resources Research*, 1–17. https://doi.org/10.1002/2014WR015498.Received

Gannon, J. P., McGuire, K. J., Bailey, S. W., Bourgault, R. R., & Ross, D. S. (2017). Lateral water flux in the unsaturated zone: A mechanism for the formation of spatial soil heterogeneity in a headwater catchment. *Hydrological Processes*, *31*(20), 3568–3579. https://doi.org/10.1002/hyp.11279

Gillin, C. P., Bailey, S. W., McGuire, K. J., & Prisley, S. P. (2015). Evaluation of lidar-derived DEMs through terrain analysis and field comparison. *Photogrammetric Engineering and Remote Sensing*, *81*(5), 387–396. https://doi.org/10.14358/PERS.81.5.387

Haught, D. R. W., & Tromp-van Meerveld, H. J. (2011). Spatial variation in transient water table responses: Differences between an upper and lower hillslope zone. *Hydrological Processes*, *25*(25), 3866–3877. https://doi.org/10.1002/hyp.8354

Heller, K., & Kleber, A. (2016). Hillslope runoff generation influenced by layered subsurface in a headwater catchment in Ore Mountains, Germany. *Environmental Earth Sciences*, *75*(11), 1–15. https://doi.org/10.1007/s12665-016-5750-y

Hinton, M. J., Schiff, S. L., & English, M. C. (1993). Physical properties governing groundwater flow in a glacial till catchment. *Journal of Hydrology*, *142*(1–4), 229–249. https://doi.org/10.1016/0022-1694(93)90012-X

Hjerdt, K. N. (2002). Deconvoluting the hydrologic response of a small till catchment: spatial variability of groundwater level and quality in relation to streamflow. *Forestry*, 204.

Hutchinson, D. G., & Moore, R. D. (2000). Throughflow variability on a forested hillslope underlain by compacted glacial till. *Hydrological Processes*, *14*(10), 1751–1766. https://doi.org/10.1002/1099-1085(200007)14:10<1751::AID-HYP68>3.0.CO;2-U

Hvorslev, M. (1951). Time Lag and Soil Permeability in Ground-Water Observations. Corps of Engineers, U.S. Army.

Jensen, C. K., McGuire, K. J., McLaughlin, D. L., & Scott, D. T. (2019). Quantifying spatiotemporal variation in headwater stream length using flow intermittency sensors. *Environmental monitoring and assessment*, *191*(4), 226

Kirchner, J. W. (2006). Getting the right answers for the right reasons: Linking measurements, analyses, and models to advance the science of hydrology. *Water Resources Research*, *42*(3), 1–5. https://doi.org/10.1029/2005WR004362

Klaus, J., & Jackson, C. R. (2018). Interflow Is Not Binary: A Continuous Shallow Perched Layer Does Not Imply Continuous Connectivity. *Water Resources Research*, *54*(9), 5921–5932. https://doi.org/10.1029/2018WR022920

Likens, G.E., 2013. Biogeochemistry of a Forested Ecosystem, 3rd ed. Springer, New York.

Lowe, W. H., & Likens, G. E. (2005). Moving headwater streams to the head of the class. *BioScience*, *55*(3), 196-197.

Mcguire, K. J., & Likens, G. E. (2011). Forest Hydrology and Biogeochemistry. *Forest Hydrology and Biogeochemistry, Synthesis of Past Research and Future Directions*, *216*(Biswas 1970), xxii, 740. https://doi.org/10.1007/978-94-007-1363-5

Nadeau, T. L., & Rains, M. C. (2007). Hydrological connectivity between headwater streams and downstream waters: How science can inform policy. *Journal of the American Water Resources Association*, *43*(1), 118–133. https://doi.org/10.1111/j.1752-1688.2007.00010.x

Neachell, E. (2014). Book Review - Environmental flows: Saving rivers in the thrid millennium. *River Research and Applications*, *30*(January), 132–133. https://doi.org/10.1002/rra

Nikroo, L., Kompani-Zare, M., Sepaskhah, A. R., & Fallah Shamsi, S. R. (2010). Groundwater depth and elevation interpolation by kriging methods in Mohr Basin of Fars province in Iran. *Environmental Monitoring and Assessment*, *166*(1–4), 387–407. https://doi.org/10.1007/s10661-009-1010-x

Nippgen, F., McGlynn, B., & Emanuel, R. (2015). The spatial and temporal evolution of contributing areas. *Water Resources Research*, (51), 4550–4573. https://doi.org/10.1002/2015WR017200.A

Panno, S. V., & Luman, D. E. (2018). Characterization of cover-collapse sinkhole morphology on a groundwater basin-wide scale using lidar elevation data: A new conceptual model for sinkhole evolution. *Geomorphology*, *318*, 1–17. https://doi.org/10.1016/j.geomorph.2018.05.013

Penna, D., Mantese, N., Hopp, L., Dalla Fontana, G., & Borga, M. (2015). Spatio-temporal variability of piezometric response on two steep alpine hillslopes. *Hydrological Processes*, *29*(2), 198–211. https://doi.org/10.1002/hyp.10140

Rau, G. C., Post, V. E. A., Shanafield, M., Krekeler, T., Banks, E. W., & Blum, P. (2019). Error in hydraulic head and gradient time-series measurements: A quantitative appraisal. *Hydrology and Earth System Sciences*, *23*(9), 3603–3629. https://doi.org/10.5194/hess-23-3603-2019

Rinderer, M., & Seibert, J. (2012). Soil Information in Hydrologic Models: Hard Data, Soft Data, and the Dialog between Experimentalists and Modelers. *Hydropedology*, 515–536. https://doi.org/10.1016/B978-0-12-386941-8.00016-2

Robinson M., & Ward, R. (2017). Sources and Components of Runoff. *Hydrology: Principles and Processes, IWA Publishing*, 236–239.

Rodhe, A., & Seibert, J. (2011). Groundwater dynamics in a till hillslope: Flow directions, gradients and delay. *Hydrological Processes*, *25*(12), 1899–1909. https://doi.org/10.1002/hyp.7946

Sills, J., Marshall, J. C., Acuña, V., Allen, D. C., Bonada, N., Boulton, A. J., ... & Negus, P. (2018). Protecting US temporary waterways. *Science*, *361*(6405), 856-857

Sophocleous, M. (2002). Interactions between groundwater and surface water: The state of the science. *Hydrogeology Journal*, *10*(1), 52–67. https://doi.org/10.1007/s10040-001-0170-8

Sprenger, M., Stumpp, C., Weiler, M., Aeschbach, W., Allen, S. T., Benettin, P., … Werner, C. (2019). The Demographics of Water: A Review of Water Ages in the Critical Zone. *Reviews of Geophysics*, *57*(3), 800–834. https://doi.org/10.1029/2018RG000633

Tromp-van Meerveld, H. J., and J. J. McDonnell (2006), Threshold relations in subsurface stormflow: 2. The fill and spill hypothesis, Water Resour. Res., 42, W02411, doi:10.1029/2004WR003800.

Tromp-van Meerveld, H. J., Seibert, J., & Peters, N. E. (2015). Hillslope-riparian-stream connectivity and flow directions at the Panola Mountain Research Watershed. *Hydrological Processes*, *29*(16), 3556–3574. https://doi.org/10.1002/hyp.10508

Vidon, P., & Smith, A. P. (2007). Upland controls on the hydrological functioning of riparian zones in glacial till valleys of the midwest. *Journal of the American Water Resources Association*, *43*(6), 1524–1539. https://doi.org/10.1111/j.1752-1688.2007.00125.x

Voeckler, H. M., Allen, D. M., & Alila, Y. (2014). Modeling coupled surface water - Groundwater processes in a small mountainous headwater catchment. *Journal of Hydrology*, *517*, 1089–1106. https://doi.org/10.1016/j.jhydrol.2014.06.015

Von Freyberg, J., Radny, D., Gall, H. E., & Schirmer, M. (2014). Implications of hydrologic connectivity between hillslopes and riparian zones on streamflow composition. *Journal of Contaminant Hydrology*, *169*(July), 62–74. https://doi.org/10.1016/j.jconhyd.2014.07.005

Wigmosta, M. S., Vail, L. W., & Lettenmaier, D. P. (1994). A distributed hydrology-vegetation model for complex terrain. *Water Resources Research*, *30*(6), 1665–1679. https://doi.org/10.1029/94WR00436

Winter, T. C., Judson W. Harvey, Franke, O. L., & Alley, W. M. (1999). *Ground Water: A Single Resource. U.S. Geological Surevy Circular 1139*. https://doi.org/10.3133/CIR1139

Wohl, E. (2017). The significance of small streams. *Frontiers of Earth Science*, *11*(3), 447-456.

Young, D., Zégre, N., Edwards, P., & Fernandez, R. (2019). Assessing streamflow sensitivity of forested headwater catchments to disturbance and climate change in the central Appalachian Mountains region, USA. *Science of the Total Environment*, *694*, 133382. https://doi.org/10.1016/j.scitotenv.2019.07.188

Zimmer, M. A., Bailey, S. W., Mcguire, K. J., & Bullen, T. D. (2013). Fine scale variations of surface water chemistry in an ephemeral to perennial drainage network. *Hydrological Processes*, *27*(24), 3438–3451. https://doi.org/10.1002/hyp.9449

Appendix A

```
#This code solves the three point problem for the water table surface and ground surface.
#Water level minimum threshold for calculating direction and gradient (m)
th = 0.050
#Calculating the gradient and direction of topography
#Matrix with x,y coordinates of each well
A <- matrix(c(1,x1,y1,1,x2,y2,1,x3,y3), 3, 3, byrow = TRUE)
colnames(A)[c(1,2,3)] <- c('A','B','C')
#This loop solves the 3-point problem and determines direction of flow for each time-step

for (i in 1:nrow(merge4)) {
#Calculates flow only if a certain amount of water (th) is detected in each well
  if (merge4[i,2] > th && merge4[i,3] > th  && merge4[i,4] > th)
  {
#Matrix of water table elevations
  b <- matrix(c(merge4[i,5], merge4[i,6], merge4[i,7]))
  gradient <- solve(A) %*% b
  #Gradient
  merge4[i,8] = (gradient[2]^2 + gradient[3]^2)^(1/2)

  #Determines azimuth for gradients in each of the four possible quandrants
  #1st quandrant
  if (gradient[2] > 0 && gradient[3] > 0) {
    merge4[i,9] = 270 - atan(gradient[3]/gradient[2])*180/pi
  }
  #2nd quandrant
  else if (gradient[2] < 0 && gradient[3] > 0) {
    merge4[i,9] = 90 - atan(gradient[3]/gradient[2])*180/pi
  }
  #3rd quandrant
  else if (gradient[2] < 0 && gradient[3] < 0) {
    merge4[i,9] = 90 - atan(gradient[3]/gradient[2])*180/pi
  }
  #4th quandrant
  else   {
    merge4[i,9] = 270 - atan(gradient[3]/gradient[2])*180/pi
  }
# U & V components
merge4[i,10] = gradient[2]
merge4[i,11] = gradient[3]
  }

  else{
  merge4[i,8] = NA
  merge4[i,9] = NA
  merge4[i,10] = NA
  merge4[i,11] = NA
  }

}
```

Figure S1: A portion of the R script used for calculating hydraulic gradients.

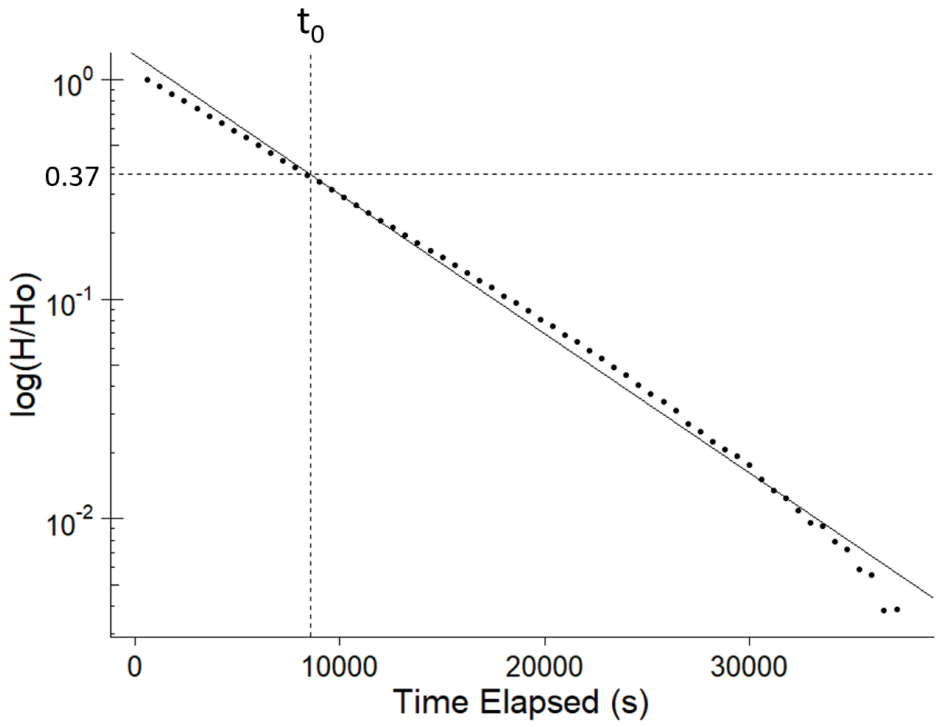

Figure S2: Time-series results for a rising-head slug test in which the recovery of water level (H) is expressed relative to the maximum displacement (Ho). The basic time lag (t_o) that corresponds to the relative head value of 0.37 used for determining saturated hydraulic conductivity. Results are plotted on a semi-log graph.